United States Department of Commerce
Technology Administration
National Institute of Standards and Technology

NIST Technical Note 1506

Electromagnetic Theory of Reverberation Chambers

David A. Hill

NIST Technical Note 1506

Electromagnetic Theory of Reverberation Chambers

David A. Hill

Radio-Frequency Technology Division
Electronics and Electrical Engineering Laboratory
National Institute of Standards and Technology
325 Broadway
Boulder, Colorado 80303-3328

December 1998

U.S. DEPARTMENT OF COMMERCE, William M. Daley, Secretary
TECHNOLOGY ADMINISTRATION, Gary R. Bachula, Acting Under Secretary for Technology
NATIONAL INSTITUTE OF STANDARDS AND TECHNOLOGY, Raymond G. Kammer, Director

CONTENTS

ELECTROMAGNETIC THEORY OF REVERBERATION CHAMBERS

David A. Hill

Radio Frequency Technology Division
National Institute of Standards and Technology
Boulder, Colorado 80303

This report presents the electromagnetic theory of reverberation chambers as applied to electromagnetic compatibility measurements. For radiated immunity measurements, mode theory and the plane-wave integral representation are useful in determining electric and magnetic field characteristics and chamber quality factor (Q). The plane-wave integral representation also provides a convenient method for describing the response of a reference antenna or a test object in a stirred field. For radiated emissions, energy conservation or electromagnetic reciprocity can be used to describe the measurement of total radiated power. Comparisons of theory and measurements are presented for chamber Q, probability density functions of fields and received power, and radiated immunity and emissions of a simple test object. Recommendations are made for improvements in statistical electromagnetic theory as applied to mechanical stirring and the statistics of immunity and emissions measurements.

Key words: electromagnetic compatibility; emissions; immunity; mode-stirred chamber; mode theory; ray theory; reverberation chamber; statistical electromagnetics.

1. INTRODUCTION

The use of reverberation chambers (also called mode-stirred chambers) for electromagnetic compatibility (EMC) measurements was first proposed in 1968 [1]. It took some time for reverberation chamber measurements to gain acceptance, but their use has increased rapidly in the past decade. The practical aspects of radiated-immunity testing in reverberation chambers were thoroughly covered in 1986 in NBS Technical Note 1092 [2], and that publication has since served as the primary reference handbook.

Because significant advances in reverberation chamber theory [3-5] and measurements [6-8] have been made since the publication of Technical Note 1092 in 1986, there is a need to update the information in that document. The amount of relevant new material has become so extensive that NIST has decided to split it into three reports. The purpose of this report is to present the electromagnetic theory of reverberation chambers, both in mathematical detail and in physical explanation. The remaining two publications cover statistical analysis [9] and practical applications [10].

Reverberation chambers are electrically large, high-Q cavities that obtain statistically uniform fields by either mechanical stirring [2] or frequency stirring [11,12]. This report will

cover only mechanical stirring because it is the more widely used method and frequency stirring is not applicable to emissions measurements. Because mechanically stirred reverberation chambers are large, complex cavities, a number of theoretical methods are needed to provide an electromagnetic characterization.

The organization of this report is as follows. Section 2 covers cavity mode theory which provides useful information on mode fields, mode excitation, and mode density, all of which impact the effectiveness of mechanical stirring. Section 3 covers a plane-wave, integral representation which allows the plane-wave coefficients to be random variables [13] for describing well-stirred fields in reverberation chambers. This statistical field theory is useful in deriving chamber Q, electric and magnetic field properties, and responses of antennas and test objects. Reverberation chambers are reciprocal devices, and Section 4 covers power conservation and reciprocity theory applied to radiated emissions measurements. Conclusions and recommendations for further study are covered in Section 5. Appendix A shows how ray theory is related multiple image theory which can provide guidelines for mechanical stirrer geometries. Appendix B gives the theory for short electric dipoles which are idealized models for electric-field probes. Appendix C gives the closely related theory for small loop antennas which are idealized models for magnetic-field probes. Appendix D relates chamber Q to chamber decay time.

2. MODE THEORY

The theory of electromagnetic cavities with separable geometries is well developed in the literature [14-16], but the application of the theory to reverberation chambers is not straightforward. Reverberation chambers typically have a large, complex stirrer (or multiple stirrers) and operate as multimode (rather than single-mode) cavities. The stirrer makes it difficult to compute the chamber fields, even for a simple source in a rectangular cavity. Also, the stirrer is typically rotated through a large number of positions so that a reverberation chamber is really an ensemble of a large number of cavities with different shapes. A simpler case where the stirrer is replaced by lateral movement of one wall of a rectangular cavity has been analyzed [17], but this geometry is not used in practice because wall movement is difficult and the resultant mode stirring is too limited. Stirrers have also been called tuners [2] to distinguish between stepped motion and continuous motion, but the term stirrer will be used throughout this report.

Despite the complexity of real reverberation chambers, the theory of empty cavity modes [18] is useful in predicting some important chamber properties, such as mode density and quality factor (Q). Also, the empty cavity modes form a complete set for expanding the fields of the same cavity when it contains source currents (on the transmitting antenna) and secondary scattering currents (on the stirrer) [19]. This section will concentrate on rectangular cavities because that is the geometry of most reverberation chambers.

2.1 Empty Cavity Modes

Consider a closed cavity of arbitrary shape with perfectly conducting walls as shown in figure 1. The interior medium (usually free space) has permittivity ε and permeability μ. The electric field $\boldsymbol{E}_p$ of the pth eigenmode satisfies the vector Helmholtz equation where the wavenumber k of the medium takes on discrete eigenvalues k_p [14]:

$$\left(\nabla^2 + k_p^2\right)\boldsymbol{E}_p = 0. \tag{1}$$

The electric field also satisfies the divergence equation

$$\nabla \bullet \boldsymbol{E}_p = 0. \tag{2}$$

On the cavity wall the tangential electric field is zero:

$$\hat{\boldsymbol{n}} \times \boldsymbol{E}_p = 0, \tag{3}$$

where ^ denotes a unit vector.

Without loss of generality, each of the electric eigenvectors $\boldsymbol{E}_p$ is chosen to be real. The corresponding magnetic eigenvector $\boldsymbol{H}_p$ is determined from Maxwell's curl equation

$$\boldsymbol{H}_p = \frac{1}{ik_p\eta} \nabla \times \boldsymbol{E}_p, \tag{4}$$

where $\eta = \sqrt{\mu/\varepsilon}$. Thus $\boldsymbol{H}_p$ is purely imaginary. Physically, the electric and magnetic fields are standing waves in phase quadrature oscillating harmonically with an angular frequency ω_p.

$$\omega_p = \frac{k_p}{\sqrt{\mu\varepsilon}}. \tag{5}$$

The total time-averaged energy U_p in a cavity mode is equal to the sum of the time-averaged electric energy U_{pe} and magnetic energy U_{pm} which are equal [14]:

$$U_p = U_{pe} + U_{pm} \quad \text{and} \quad U_{pe} = U_{pm}. \tag{6}$$

The time-averaged electric and magnetic energies are defined as volume integrals [20]:

$$U_{pe} = \frac{\varepsilon}{2} \iiint_V \left|E_p\right|^2 \mathrm{d}V \quad \text{and} \quad U_{pm} = \frac{\mu}{2} \iiint_V \left|H_p\right|^2 \mathrm{d}V. \tag{7}$$

(The coefficients of the integrals in eq (7) involve factors of ½ rather than ¼ because we follow Harrington's notation [20] of using RMS values rather than peak values for phasors.)

Numerical methods are required to solve eqs (1) through (3) for the eigenvalues and eigenvectors of cavities of general shape. For separable geometries, such as rectangular, circular cylindrical, or spherical, the eigenfunctions and eigenvalues are well known [21]. Spherical and circular cylindrical cavities are not of much interest for reverberation chambers because the curved surfaces can produce caustics (focusing of rays) that make it difficult to obtain spatial field uniformity. Complex cavity shapes have been studied numerically in the physics community to study chaotic mode fields [22], and the relevance of this work to reverberation

chambers remains an open question. In this report, we will concentrate on the rectangular cavity because it is the primary geometry in use, it has been shown to produce good field uniformity with stirring, and it is the best understood cavity shape.

The geometry for an empty rectangular cavity is shown in figure 2. There is no preferred axis, and all cavity modes can be written as either transverse electric (TE) or transverse magnetic (TM) to any of the three coordinate axes. To follow the usual convention in the literature [18-20], we choose to construct modes that are either TE or TM to the z direction. The electric fields of the TE and TM modes can be written in the following forms [19]:

$$E_p^{\mathrm{TE}}(r) = -\hat{x}k_y\phi_p^x(r) + \hat{y}k_x\phi_p^y(r) \tag{8}$$

and

$$E_p^{\mathrm{TM}} = -\hat{x}k_xk_y\phi_p^x(r) - \hat{y}k_yk_z\phi_p^y(r) + \hat{z}(k_x^2 + k_y^2)\phi_p^z(r), \tag{9}$$

where

$$\phi_p^x(r) = \frac{\varepsilon_p}{\sqrt{abc}}\cos(k_x x)\sin(k_y y)\sin(k_z z),$$

$$\phi_p^y(r) = \frac{\varepsilon_p}{\sqrt{abc}}\sin(k_x x)\cos(k_y y)\sin(k_z z), \tag{10}$$

$$\phi_p^z(r) = \frac{\varepsilon_p}{\sqrt{abc}}\sin(k_x x)\sin(k_y y)\cos(k_z z),$$

and

$$k_x = \frac{l\pi}{a}, k_y = \frac{m\pi}{b}, k_z = \frac{n\pi}{c},$$

$$\varepsilon_p = \begin{cases} 2 & \text{for } l = 0, m = 0, \text{or } n = 0 \\ \sqrt{8} & \text{for } l, m, n \neq 0. \end{cases} \tag{11}$$

The modal subscript p is shorthand for the nonnegative integers l, m, and n. Only one of these three integers can equal zero for any one mode. The time dependence, $\exp(-i\omega_p t)$, is suppressed. At this point, the normalization of the modes is arbitrary, but the above normalization is useful in deriving the Green's function for the source problem [19].

The expressions for the electric field of the TE and TM modes in eqs (8) and (9) are consistent with other results in the literature [18,20,21], and the corresponding magnetic-field expressions can be obtained by substituting eq (8) or (9) into eq (4). Equation (8) shows that the

z component of the electric field is zero for TE modes. Equations (4) and (9) show that the z component of the magnetic field is zero for TM modes.

2.2 Fields of Current Sources

In this section we consider the fields excited by a source current distribution $\boldsymbol{J}(\boldsymbol{r}')$ in a rectangular cavity as shown in figure 3. The current and the induced fields have a time dependence $\exp(-i\omega t)$ which is suppressed in the rest of this report. The induced electric field $\boldsymbol{E}(\boldsymbol{r})$ can be written as an integral over the source volume:

$$\boldsymbol{E}(\boldsymbol{r}) = -i\omega\mu \iiint_{V_s} \overline{\boldsymbol{G}}(\boldsymbol{r},\boldsymbol{r}') \bullet \boldsymbol{J}(\boldsymbol{r}')\,\mathrm{d}V', \tag{12}$$

where $\overline{\boldsymbol{G}}$ is the dyadic Green's function which satisfies the differential equation [19]

$$\nabla \times \nabla \times \overline{\boldsymbol{G}}(\boldsymbol{r},\boldsymbol{r}') - k^2 \overline{\boldsymbol{G}}(\boldsymbol{r},\boldsymbol{r}') = \overline{\boldsymbol{I}}\,\delta(\boldsymbol{r}-\boldsymbol{r}'), \tag{13}$$

$\overline{\boldsymbol{I}}$ is the identity dyad, δ is the three-dimensional delta function, and $k = \omega\sqrt{\mu\varepsilon}$ is the wavenumber of the medium. The dyadic Green's function also satisfies the boundary condition,

$$\hat{\boldsymbol{n}} \times \overline{\boldsymbol{G}}(\boldsymbol{r},\boldsymbol{r}') = 0, \tag{14}$$

for either $\boldsymbol{r}$ or $\boldsymbol{r}'$ on the cavity wall.

The dyadic Green's function can be constructed from the source-free cavity modes in eqs (8) and (9) and a set of functions that have nonzero divergence and zero curl [19]. This set of functions is necessary in order satisfy Maxwell's equations in the source region. The result for $\overline{\boldsymbol{G}}$ [19] can be written in terms of the ϕ functions which were defined in eq (10):

$$\begin{aligned}
\overline{\boldsymbol{G}}(\boldsymbol{r},\boldsymbol{r}') = \sum_{l=0}^{\infty}\sum_{m=0}^{\infty}\sum_{n=0}^{\infty} \frac{1}{k^2(k_p^2-k^2)} \{ & \hat{x}\hat{x}(k^2-k_x^2)\phi_p^x(\boldsymbol{r})\phi_p^x(\boldsymbol{r}') \\
& - \hat{x}\hat{y}k_xk_y\phi_p^x(\boldsymbol{r})\phi_p^y(\boldsymbol{r}') - \hat{x}\hat{z}k_xk_z\phi_p^x(\boldsymbol{r})\phi_p^z(\boldsymbol{r}') \\
& - \hat{y}\hat{x}k_yk_x\phi_p^y(\boldsymbol{r})\phi_p^x(\boldsymbol{r}') + \hat{y}\hat{y}(k^2-k_y^2)\phi_p^y(\boldsymbol{r})\phi_p^y(\boldsymbol{r}') \\
& - \hat{y}\hat{z}k_yk_z\phi_p^y(\boldsymbol{r})\phi_p^z(\boldsymbol{r}') - \hat{z}\hat{x}k_zk_x\phi_p^z(\boldsymbol{r})\phi_p^x(\boldsymbol{r}') \\
& - \hat{z}\hat{y}k_zk_y\phi_p^z(\boldsymbol{r})\phi_p^y(\boldsymbol{r}') + \hat{z}\hat{z}(k^2-k_z^2)\phi_p^z(\boldsymbol{r})\phi_p^z(\boldsymbol{r}') \}.
\end{aligned} \tag{15}$$

This result is in agreement with the dyadic Green's function in a more recent publication [17].

Several comments regarding the form of $\overline{\boldsymbol{G}}$ in eq (15) are in order. Each of the nine dyadic terms in the triple summation satisfies the wall boundary condition in eq (14), so $\overline{\boldsymbol{G}}$ automatically satisfies eq (14). The convergence of the triple sum in eq (15) becomes very slow as the observation point $\boldsymbol{r}$ approaches the source point $\boldsymbol{r}'$. In fact the sums do not converge when $\boldsymbol{r} = \boldsymbol{r}'$ because $\overline{\boldsymbol{G}}$ is singular. The details of the singularity of $\overline{\boldsymbol{G}}$ and the evaluation of the electric field from eq (12) have been thoroughly studied [23], and the convergence of the sums can be

improved by converting eq (15) to a sum of rays and modes [19]. The relationship between rays and modes will be discussed further in Appendix A.

Because of the factor $(k_p^2 - k^2)^{-1}$, eq (15) also has singularities at all of the resonant frequencies determined by $k = k_p$ or $\omega = \omega_p$. These singularities occur only for lossless cavities where the quality factor Q is infinite. For finite, but large, values of cavity Q, an approximate correction [14] to eq (15) can be obtained by replacing k_p by $k_p(1 - \frac{i}{2Q})$ or ω_p by $\omega_p(1 - \frac{i}{2Q})$. This replacement keeps the modal terms finite for real values of k or ω and yields a half-power modal bandwidth of ω_p/Q. If Q is mode dependent, then the modal Q_p should be used in the above replacements, and the half-power modal bandwidth is ω_p/Q_p.

The polarization properties of fields produced by currents within the cavity (on either source antenna or the stirrer) can be determined from eq (15) since it is written in nine separate dyads. For example, consider the fields produced by z-directed currents, $\boldsymbol{J}(\boldsymbol{r}') = \hat{z}J_z(\boldsymbol{r}')$, as would be supported by a z-directed linear antenna. Then eq (12) would become

$$E(\boldsymbol{r}) = -i\omega\mu \iiint_{V_s} G(\boldsymbol{r}, \boldsymbol{r}') \bullet \hat{z}J_z(\boldsymbol{r}')\mathrm{d}V'. \tag{16}$$

The vector properties of the electric field are determined by the following dot product that extracts three of the nine terms in G:

$$\begin{aligned} G(\boldsymbol{r}, \boldsymbol{r}') \bullet \hat{z} = \sum_{l=0}^{\infty}\sum_{m=0}^{\infty}\sum_{n=0}^{\infty} \frac{1}{k^2(k_p^2 - k^2)} \{ & -\hat{x}k_x k_z \phi_p^x(\boldsymbol{r})\phi_p^z(\boldsymbol{r}') \\ & - \hat{y}k_y k_z \phi_p^y(\boldsymbol{r})\phi_p^z(\boldsymbol{r}') + \hat{z}(k^2 - k_z^2)\phi_p^z(\boldsymbol{r})\phi_p^z(\boldsymbol{r}')\}. \end{aligned} \tag{17}$$

The dot product in eq (17) includes all three vector components; so the electric field in eq (16) will also include all three vector components. Even though z-directed currents will excite all three components of the electric field, they do not provide a thorough mode excitation of the cavity. The way to see this is to derive the magnetic field from Maxwell's curl equation:

$$\boldsymbol{H} = \frac{1}{ik\eta} \nabla \times \boldsymbol{E}. \tag{18}$$

If eqs (16) and (17) are substituted into eq (18), it is found that $H_z = 0$. This is because z-directed currents do excite TM modes of the form given by eq (9), but do not excite TE modes of the form given by eq (8). Either x-directed or y-directed currents will excite TE modes.

Normally an effective asymmetrical stirrer will support all three components of electric current and will excite both TE and TM modes. The task of computing currents on electrically large, complex stirrers is extremely difficult (particularly for a large number or orientations); so the currents needed to evaluate the electric field in eq (12) are generally unknown. Some two-dimensional stirrer calculations have been done [24], but numerical methods are only beginning to be applied to realistic three-dimensional cavities with large stirrers. However, the rectangular-

cavity Green's function can be used to analyze frequency stirring in rectangular cavities [25] where no mechanical stirrer is present.

2.3 Mode Number and Density

The source-free modes of an empty rectangular cavity have been thoroughly studied by Liu, Chang, and Ma [18], and their results for mode number and density are summarized in this section. For the rectangular cavity shown in figure 2, the eigenvalues (wavenumbers) k_p are determined from

$$k_{lmn}^2 = \omega_{lmn}^2 \mu\varepsilon = \left(\frac{l\pi}{a}\right)^2 + \left(\frac{m\pi}{b}\right)^2 + \left(\frac{n\pi}{c}\right)^2, \tag{19}$$

where l, m, and n are nonnegative integers. The shorthand subscript p will be replaced by the full designation lmn in this section to make the mode identification more explicit.

In mode counting, the mode degeneracies need to be considered. When none of the indicies lmn is zero, there are two types of modes, TE_{lmn} and TM_{lmn}, for each eigenvalue. So the mode degeneracy is 2. When $l = 0$, only a TE_{0mn} mode exists for each eigenvalue. When $m = 0$, only a TE_{l0n} mode exists for each eigenvalue. When $n = 0$, only a TM_{lm0} mode exists for each eigenvalue. The forms of the electric fields of the TE and TM modes are given in eqs (8) and (9). For mode counting, we designate $N(k)$ as the number of modes with eigenvalues k_{lmn} less than or equal to k. This total number of modes is the sum of the number of modes of each of the above types:

$$\begin{aligned} N(k) &= N_1(k) + N_2(k) + N_3(k) + N_4(k) + N_5(k) \\ &= 2N_1(k) + N_3(k) + N_4(k) + N_5(k), \end{aligned} \tag{20}$$

where N_1 represents TM_{lmn} modes, N_2 ($= N_1$) represents TE_{lmn} modes, N_3 represents TM_{lm0} modes, N_4 represents TE_{0mn} modes, and N_5 represents TE_{l0n} modes. The notation and properties of the five mode types are summarized in table 1.

Equation (20) can be evaluated numerically by mode counting, but simple analytical approximations are also available. The actual mode number is a discontinuous function of k, but the best smooth approximation N_s is [18]

$$N_s(k) = \frac{abc}{3\pi^2}k^3 - \frac{a+b+c}{2\pi}k + \frac{1}{2}. \tag{21}$$

The first term on the right side of eq (21) is Weyl's classical approximation N_W, which is valid for cavities of general shape and can be written in terms of the volume V:

$$N_W(k) = \frac{Vk^3}{3\pi^2}. \tag{22}$$

The extra terms in eq (21) are specific to the rectangular shape. The mode numbers in eqs (21) and (22) can also be written as functions of frequency f:

$$N_s(f) = \frac{8\pi}{3} abc \frac{f^3}{v^3} - (a+b+c)\frac{f}{v} + \frac{1}{2} \tag{23}$$

and

$$N_W(f) = \frac{8\pi V}{3} \frac{f^3}{v^3}, \tag{24}$$

where v is the speed of light in the medium (usually free space). Equations (21) through (24) are asymptotic high-frequency approximations that are valid when the cavity dimensions are somewhat greater than a half wavelength.

Numerical results for N (by computer counting), N_s, and N_W are shown in figure 4 for the NIST reverberation chamber (a = 2.74 m, b = 3.05 m, and c = 4.57 m). The extra terms in N_s improve the agreement obtained with Weyl's formula. The smooth mode density $D_s(f)$ is also shown in figure 4. It is obtained by differentiating eq (23):

$$D_s(f) = \frac{dN_s(f)}{df} = 8\pi abc \frac{f^2}{v^3} - \frac{a+b+c}{v}. \tag{25}$$

The Weyl approximation again equals the first term:

$$D_W(f) = \frac{dN_W(f)}{df} = 8\pi V \frac{f^2}{v^3}. \tag{26}$$

The mode density is an important chamber design parameter because it determines how many modes are present in a small bandwidth about a given frequency. For example, figure 4 shows that the NIST chamber has a mode density somewhat greater than 1 mode per megahertz at a frequency of 200 MHz. Experience has shown that the NIST chamber provides adequate performance at frequencies above 200 MHz, but not below 200 MHz where the mode density is too low to obtain spatial field uniformity [2].

3. PLANE-WAVE, INTEGRAL REPRESENTATION

Deterministic mode theory, as discussed in the previous section, is useful in determining empty-cavity properties, but it is not convenient for predicting the response of a receiving antenna or test object in a mechanically stirred reverberation chamber. Since many stirrer positions are employed in reverberation chamber measurements, some type of statistical method [4] is required to determine the statistics of antenna or test object response. At the same time, it is important to ensure that the associated electromagnetic theory is consistent with Maxwell's equations.

The purpose of this section is to present a plane-wave, integral representation for the electric and magnetic fields that satisfies Maxwell's equations and also includes the statistical properties expected for a well-stirred field [13]. The statistical nature of the fields is introduced through the plane-wave coefficients that are taken to be random variables with fairly simple statistical properties. Because the theory uses only propagating plane waves, it is fairly easy to use to calculate the responses of test objects or reference antennas.

Section 3.1 presents the basic plane-wave integral theory and derivations of important field properties. Section 3.2 includes derivations of the responses of antennas or test objects to the statistical field. Section 3.3 derives probability density functions for the fields and test object responses. Section 3.4 analyzes the loss mechanisms and the Q of a reverberation chamber.

3.1 Electric and Magnetic Field Properties

A typical geometry for an immunity measurement in a reverberation chamber is shown in figure 5. A transmitting antenna radiates cw fields, and the mechanical stirrer (or multiple stirrers) is rotated to generate a statistically uniform field. The test volume can occupy a fairly large portion of the chamber volume.

The electric field $\boldsymbol{E}$ at location $\boldsymbol{r}$ in a source-free, finite volume can be represented as an integral of plane waves over all real angles [26]

$$\boldsymbol{E}(\boldsymbol{r}) = \iint_{4\pi} \boldsymbol{F}(\Omega) \exp(i\boldsymbol{k} \bullet \boldsymbol{r})\, \mathrm{d}\Omega, \tag{27}$$

where the solid angle Ω is shorthand for the elevation and azimuth angles, α and β, and $d\Omega = \sin\alpha\, \mathrm{d}\alpha\, \mathrm{d}\beta$. The $\exp(-i\omega t)$ time dependence is suppressed. The vector wavenumber $\boldsymbol{k}$ is

$$\boldsymbol{k} = -k(\hat{x}\sin\alpha\cos\beta + \hat{y}\sin\alpha\sin\beta + \hat{z}\cos\alpha). \tag{28}$$

The angular spectrum $\boldsymbol{F}(\Omega)$ can be written

$$\boldsymbol{F}(\Omega) = \hat{\alpha}F_{\alpha}(\Omega) + \hat{\beta}F_{\beta}(\Omega), \tag{29}$$

where $\hat{\alpha}$ and $\hat{\beta}$ are unit vectors that are orthogonal to each other and to $\boldsymbol{k}$. Both F_{α} and F_{β} are complex and can be written in terms of their real and imaginary parts:

$$F_{\alpha}(\Omega) = F_{\alpha r}(\Omega) + iF_{\beta r}(\Omega) \quad \text{and} \quad F_{\beta}(\Omega) = F_{\beta r}(\Omega) + iF_{\beta i}(\Omega). \tag{30}$$

The geometry for a plane-wave component is shown in figure 6.

The electric field in eq (27) satisfies Maxwell's equations because each plane-wave component satisfies Maxwell's equations. For a spherical volume, the representation in eq (27) can be shown to be complete because it is equivalent to the rigorous spherical-wave expansion [27]. For a non-spherical volume, the plane-wave expansion can be analytically continued outward from a spherical volume, but the general conditions under which the analytic

continuation is valid have yet to be established. In this report, we assume that the volume is selected so that eq (27) is valid.

For a statistical field as generated in a reverberation chamber, the angular spectrum $F(\Omega)$ is taken to be a random variable (which depends on stirrer position). For derivation of many of the important field quantities, the probability density function of the angular spectrum is not required, and it is sufficient to specify certain means and variances. In a typical reverberation chamber measurement, the statistical ensemble is generated by rotating the stirrer (or stirrers). In this report, $< >$ represents an ensemble average over stirrer position. The starting point for the statistical analysis is to select statistical properties for the angular spectrum that are representative of a well-stirred field which would be obtained in an electrically large, multimode chamber with a large, effective stirrer [2]. Appropriate statistical assumptions for such a field are as follows:

$$< F_\alpha(\Omega) > = < F_\beta(\Omega) > = 0, \tag{31}$$

$$< F_{\alpha r}(\Omega_1) F_{\alpha i}(\Omega_2) > = < F_{\beta r}(\Omega_1) F_{\beta i}(\Omega_2) > =$$

$$< F_{\alpha r}(\Omega_1) F_{\beta r}(\Omega_2) > = < F_{\alpha r}(\Omega_1) F_{\beta i}(\Omega_2) > = \tag{32}$$

$$< F_{\alpha i}(\Omega_1) F_{\beta r}(\Omega_2) > = < F_{\alpha i}(\Omega_1) F_{\beta i}(\Omega_2) > = 0,$$

and

$$\begin{aligned} &< F_{\alpha r}(\Omega_1) F_{\alpha r}(\Omega_2) > = < F_{\alpha i}(\Omega_1) F_{\alpha i}(\Omega_2) > = \\ &< F_{\beta r}(\Omega_1) F_{\beta r}(\Omega_2) > = < F_{\beta i}(\Omega_1) F_{\beta i}(\Omega_2) > = C_E \delta(\Omega_1 - \Omega_2), \end{aligned} \tag{33}$$

where δ is the Dirac delta function and C_E is a constant with units of $(V/m)^2$.

The mathematical reasons for the assumptions, eqs (31) through (33), will become clear when the field properties are derived, but the physical justifications are as follows. Since the angular spectrum is a result of many rays or bounces with random phases, the mean value ought to be zero, as indicated in eq (31). Since multipath scattering changes the phase and rotates the polarization many times, angular spectrum components with orthogonal polarizations or quadrature phase ought to be uncorrelated, as indicated in eq (32). Since angular spectrum components arriving from different directions have taken very different multiple scattering paths, they ought to be uncorrelated as indicated by the delta function on the right side of eq (33). The coefficient C_E of the delta function is proportional to the square of the electric field strength as will be shown later. The following useful relationships can be derived from eqs (32) and (33):

$$< F_\alpha(\Omega_1) F_\beta(\Omega_2) > = 0, \tag{34}$$

and

$$< F_\alpha(\Omega_1) F_\alpha^*(\Omega_2) > = < F_\beta(\Omega_1) F_\beta^*(\Omega_2) > = 2C_E \delta(\Omega_1 - \Omega_2), \tag{35}$$

where * denotes complex conjugate.

A number of field properties can be derived from eqs (27) and (31) through (35). Consider first the mean value of the electric field <*E*>, which can be derived from eqs (27) and (31):

$$< E(r) > = \iint_{4\pi} < F(\Omega) > \exp(ik \bullet r)\, d\Omega = 0. \tag{36}$$

Thus the mean value of the electric field is zero because the mean value of the angular spectrum is zero. This result is expected for a well-stirred field which is the sum of a large number of multipath rays with random phases.

The square of the absolute value of the electric field is important because it is proportional to the electric energy density [5]. From eq (27), the square of the absolute value of the electric field can be written as a double integral:

$$| E(r) |^2 = \iint_{4\pi} \iint_{4\pi} F(\Omega_1) \bullet F^*(\Omega_2) \exp[i(k_1 - k_2) \bullet r]\, d\Omega_1\, d\Omega_2. \tag{37}$$

The mean value of eq (37) can be derived by applying eqs (34) and (35) to the integrand:

$$< | E(r) |^2 > = 4C_E \iint_{4\pi} \iint_{4\pi} \delta(\Omega_1 - \Omega_2) \exp[i(k_1 - k_2) \bullet r] d\Omega_1 d\Omega_2. \tag{38}$$

One integration in eq (38) can be evaluated by using the sampling property of the delta function, and the second integration is easily evaluated to obtain the final result:

$$< | E(r) |^2 > = 4C_E \iint_{4\pi} d\Omega_2 = 16\pi C_E \equiv E_0^2. \tag{39}$$

Thus the mean-square value of the electric field is E_0^2 and is independent of position. This is the field uniformity property of an ideal reverberation chamber; it applies to the ensemble average of the squared electric field and has been verified experimentally with an array of electric-field probes [2],[8]. For convenience throughout the remainder of this report, C_E is defined in terms of the mean-square value of the electric field as indicated in eq (39).

By a similar derivation, the mean-square values of the rectangular components of the electric field can be derived:

$$< | E_x |^2 > = < | E_y |^2 > = < | E_z |^2 > = \frac{E_0^2}{3}. \tag{40}$$

This is the isotropy property of an ideal reverberation chamber, and it has been verified with three-axis, electric-field probes [2],[8].

The magnetic field H can be derived by applying Maxwell's curl equation to eq (27):

$$H(r) = \frac{1}{i\omega\mu} \nabla \times E(r) = \frac{1}{\eta} \iint_{4\pi} \hat{k} \times F(\Omega) \exp(ik \bullet r) \, d\Omega. \tag{41}$$

Applying eq (31) to eq (41) shows that the mean value of the magnetic field is zero:

$$< H(r) > = \frac{1}{\eta} \iint_{4\pi} \hat{k} \times < F(\Omega) > \exp(ik \bullet r) \, d\Omega = 0. \tag{42}$$

The square of the magnitude of the magnetic field can be written

$$| H(r) |^2 = \frac{1}{\eta^2} \iint_{4\pi} \iint_{4\pi} \left[\hat{k}_1 \times F(\Omega_1)\right] \bullet \left[\hat{k}_2 \times F^*(\Omega_2)\right] \exp[i(k_1 - k_2) \bullet r] \, d\Omega_1 \, d\Omega_2 . \tag{43}$$

The derivation of the mean-square value follows closely that of the electric field, and the result is

$$< | H(r) |^2 > = \frac{E_0^2}{\eta^2}. \tag{44}$$

Thus the mean-square magnetic field also exhibits spatial uniformity, and the value is related to the mean-square electric field by the square of the free-space impedance:

$$< | H(r_1) |^2 > = \frac{< | E(r_2) |^2 >}{\eta^2}, \tag{45}$$

where r_1 and r_2 are arbitrary locations. This free-space relationship has been demonstrated experimentally by using electric and magnetic field probes [2].

The energy density W can be written [20]

$$W(r) = \frac{1}{2} [\varepsilon \, | E(r) |^2 + \mu \, | H(r) |^2]. \tag{46}$$

The mean value can be obtained from eqs (39), (44), and (46):

$$< W(r) > = \frac{1}{2} [\varepsilon < | E(r) |^2 > + \mu < | H(r) |^2 >] = \varepsilon E_0^2 . \tag{47}$$

Thus the average value of the energy density is also independent of position.

The power density or Poynting vector S can be written [20]

$$S(r) = E(r) \times H^*(r). \tag{48}$$

From eqs (27), (42), and (48), the mean of the power density can be written

$$< S(r) >= \frac{1}{\eta} \iint_{4\pi} \iint_{4\pi} < F(\Omega_1) \times [k_2 \times F^*(\Omega_2)] > \exp[i(k_1 - k_2) \bullet r] \, d\Omega_1 \, d\Omega_2 . \tag{49}$$

The expectation in the integrand can be evaluated from vector identies and eqs (34) and (35):

$$< F(\Omega_1) \times [\hat{k}_2 \times F(\Omega_2)] >= \hat{k}_2 \frac{E_0^2}{4\pi} \delta(\Omega_1 - \Omega_2). \tag{50}$$

The right side of eq (49) can now be evaluated from eq (50) and the sampling property of the delta function:

$$< S(r) >= \frac{E_0^2}{4\pi\eta} \iint_{4\pi} \hat{k}_2 d\Omega_2 = 0. \tag{51}$$

A physical interpretation of eq (51) is that each plane wave carries equal power in a different direction so that the vector integration over 4π steradians is zero. This result is important because it shows that power density is not the proper quantity for characterizing field strength in reverberation chambers. The mean value of energy density as given by eq (47) is an appropriate positive scalar quantity that could be used. Another possibility is to define a positive scalar quantity S that has units of power density and is proportional to the mean energy density:

$$S = v < W >= \frac{E_0^2}{\eta}, \tag{52}$$

where $v = 1/\sqrt{\mu\varepsilon}$. For lack of a better term, S will be called scalar power density in the rest of this report. This quantity could be used to compare with uniform-field, plane-wave testing where power density, rather than field strength, is sometimes specified.

To this point, field properties at a point have been considered. Real antennas and test objects have significant spatial extent, and the spatial correlation function [28] of the fields is important in understanding responses of extended objects in reverberation chambers [29]. The spatial correlation function $\rho(r_1,r_2)$ of the electric field can be defined as

$$\rho(r_1, r_2) = \frac{< E(r_1) \bullet E^*(r_2) >}{\sqrt{<| E(r_1) |^2 >< | E(r_2) |^2 >}}, \tag{53}$$

where r_1 and r_2 are two arbitrary locations. The numerator of eq (53) is the mutual coherence function which has been used to describe wave propagation in random media [30]. The denominator of eq (53) can be evaluated from eq (39), and the numerator can be evaluated from eqs (27), (34), and (35) so that the final result is [28]

$$\rho(r_1, r_2) = \frac{\sin(k\,|\,r_1 - r_2\,|)}{k\,|\,r_1 - r_2\,|}. \tag{54}$$

The identical correlation function has been derived from cavity mode theory [4] and radiative transfer theory [31] and has been checked experimentally [29]. The same correlation function can be derived for the magnetic field, and it also applies to acoustic reverberation chambers [32]. A correlation length l_c can be defined as the separation corresponding to the first zero in eq (54):

$$kl_c = \pi \quad \text{or} \quad l_c = \pi / k = \lambda / 2, \tag{55}$$

where λ is the wavelength in the medium.

An angular correlation function $\rho(\hat{s}_1, \hat{s}_2)$ can be defined as

$$\rho(\hat{s}_1, \hat{s}_2) = \frac{< E_{s1}(r) E_{s2}(r) >}{\sqrt{<|\,E_{s1}(r)\,|^2><|\,E_{s2}(r)\,|^2>}}, \tag{56}$$

where the two electric field components are defined as

$$E_{s1}(r) = \hat{s}_1 \bullet E(r) \quad \text{and} \quad E_{s2}(r) = \hat{s}_2 \bullet E(r) \tag{57}$$

and $\hat{s}_1$ and $\hat{s}_2$ are unit vectors separated by an angle γ as shown in figure 7. From eq (40), the denominator of eq (56) is found to equal $E_0^2 / 3$. The numerator of eq (56) is evaluated from eqs (27), (34), and (35), and the result for the angular correlation function is

$$\rho(\hat{s}_1, \hat{s}_2) = \hat{s}_1 \bullet \hat{s}_2 = \cos\gamma. \tag{58}$$

This result is independent of position r. The same angular correlation function can be derived for magnetic field components. Equation (58) shows that the three rectangular components of the electric field are uncorrelated, and this is consistent with the theory of Kostas and Boverie [33].

3.2 Antenna or Test-Object Response

Consider now a receiving antenna or a test object placed in the test volume. The simplest case of a lossless, impedance-matched antenna will be considered first. The received signal can be written as an integral over incidence angle by analogy with Kerns's plane-wave, scattering-matrix theory [34]. The received signal could be a current, a voltage, or a waveguide mode coefficient, but the general formulation remains the same. Consider the received signal to be a current I induced in a matched load. For an antenna located at the origin, the current can be written as a dot product of the angular spectrum with a receiving function $S_r(\Omega)$ integrated over angle:

$$I = \iint_{4\pi} \boldsymbol{S}_r(\Omega) \bullet \boldsymbol{F}(\Omega)\, \mathrm{d}\Omega, \tag{59}$$

where the receiving function can be written in terms of two components,

$$\boldsymbol{S}_r(\Omega) = \hat{\alpha} S_{r\alpha}(\Omega) + \hat{\beta} S_{r\beta}(\Omega). \tag{60}$$

In general, $S_{r\alpha}$ and $S_{r\beta}$ are complex, so the antenna can have arbitrary polarization, such as linear or circular. For example, a z-directed linear antenna with linear polarization would have $S_{r\beta}(\Omega) = 0$. A circularly polarized antenna would have $S_{r\beta}(\Omega) = \pm i S_{r\alpha}(\Omega)$ for right- or left-hand circular polarization.

The mean value of the current I can be shown to be zero from eqs (31) and (59):

$$< I >= \iint_{4\pi} \boldsymbol{S}_r(\Omega) \bullet < \boldsymbol{F}(\Omega) > \mathrm{d}\Omega = 0. \tag{61}$$

The absolute value of the square of the current is important because it is proportional to received power P_r:

$$P_r = |I|^2 R_r = R_r \iint_{4\pi} \iint_{4\pi} [\boldsymbol{S}_r(\Omega_1) \bullet \boldsymbol{F}(\Omega_1)][\boldsymbol{S}_r^*(\Omega_2) \bullet \boldsymbol{F}^*(\Omega_2)]\, \mathrm{d}\Omega_1\, \mathrm{d}\Omega_2, \tag{62}$$

where the radiation resistance R_r of the antenna is also equal to the real part of the matched load impedance. The mean value of the received power can be determined from eqs (34), (35), and (62):

$$< P_r >= <|I|^2> R_r = \frac{E_0^2}{2} \frac{R_r}{4\pi} \iint_{4\pi} [|S_{r\alpha}(\Omega_2)|^2 + |S_{r\beta}(\Omega_2)|^2]\, \mathrm{d}\Omega_2. \tag{63}$$

The physical interpretation of eq (63) is that the ensemble average of received power is equal to an average incidence angle (Ω_2) and polarization (α and β components).

The integrand of eq (63) can be related to the effective area of an isotropic antenna $\lambda^2/4\pi$ and the antenna directivity $D(\Omega_2)$ by [35]

$$\eta R_r [|S_{r\alpha}(\Omega_2)|^2 + |S_{r\beta}(\Omega_2)|^2] = \frac{\lambda^2}{4\pi} D(\Omega_2). \tag{64}$$

Substitution of eq (64) into eq (63) yields

$$< P_r >= \frac{1}{2} \frac{E_0^2}{\eta} \frac{\lambda^2}{4\pi} \frac{1}{4\pi} \iint_{4\pi} D(\Omega_2) d\Omega_2. \tag{65}$$

The integral in eq (65) is known because the average (over Ω_2) of D is 1. Thus the final result for the average received power is

$$< P_r >= \frac{1}{2} \frac{E_0^2}{\eta} \frac{\lambda^2}{4\pi}. \tag{66}$$

The physical interpretation of eq (66) is that the average received power is the product of the scalar power density E_0^2 / η times the effective area $\lambda^2 / 4\pi$ of an isotropic antenna times a polarization mismatch factor of one half [36]. This result is independent of the antenna directivity and is consistent with the reverberation chamber analysis [37] of Corona et al. Some of the earlier data indicated that eq (66) was in better agreement with measurements if the one half polarization mismatch factor was omitted [2]. However, more recent comparisons of antenna received power with field-probe data [8] and with a well-characterized test object [38] support the inclusion of the factor of one half. Consequently, the polarization mismatch factor needs to be included to be in agreement with theory and with most measured data. Traditionally, linearly polarized antennas have been used as reference antennas in reverberation chambers, but this analysis suggests that circularly polarized antennas are also appropriate. Experimental data with circularly polarized would be useful for confirming this theoretical result. The special cases of an electrically short dipole (electric-field probe) and an electrically small loop (magnetic-field probe) are discussed in Appendices B and C.

The preceding analysis can be extended to the case of a real antenna with loss and impedance mismatch by using Tai's theory [36]. The effective area A_e can be generalized to

$$A_e(\Omega) = \frac{\lambda^2}{4\pi} D(\Omega) p m \eta_a , \tag{67}$$

where p is the polarization mismatch, m is the impedance mismatch, and η_a is the antenna efficiency. All three quantities, p, m, and η_a, are real and can vary between 0 and 1. The average of A_e over incidence angle and polarization can be written [37]

$$< A_e >= \frac{\lambda^2}{8\pi} m \eta_a . \tag{68}$$

The average received power is

$$< P_r >= \frac{E_0^2}{\eta} < A_e >, \tag{69}$$

where E_0^2 / η can again be interpreted as the average scalar power density.

Test objects can be thought of as lossy, impedance-mismatched antennas, so eq (69) also applies to test objects as long as terminals with linear loads can be identified. This theory has been used to predict the responses of an apertured coaxial line [39], an apertured rectangular box [5], and a microstrip transmission line [38,40] as compared to a reference antenna in a reverberation chamber. Good agreement with measurements has been obtained in each case.

The microstrip example is a good illustration of the use of the above theory. The response of terminated microstrip transmission line was computed using the above theory and measured in the NIST reverberation chamber [40] using the setup shown in figure 8. A comparison of theory and measurements is shown in figure 9 for frequencies from 200 to 2000 MHz. The plotted quantity is the ratio of the average power received by the reference antenna to the average power received by the microstrip line in decibels. (This ratio is sometimes called shielding effectiveness in decibels.) The theoretical ratio is $20\log_{10}[(\lambda^2/8\pi)/<A_e>]$, where $\lambda^2/8\pi$ is the theoretical average effective area of the reference antenna and $<A_e>$ is the average effective area of the microstrip transmission line. The measurements were performed on three different physical models, and the "bottom feed" microstrip line best fits the theoretical model. Hence it has the best agreement with theory. Even that measured curve has a small negative bias which is probably due to impedance mismatch in the reference antenna which was not taken into account. The actual reference antenna was a log periodic dipole array below 1000 MHz and a broadband ridged horn above 1000 MHz.

3.3 Probability Density Functions

The statistical assumptions for the angular spectrum in eqs (31) through (33) have been used to derive a number of useful ensemble averages in sections 3.1 and 3.2. These results have not required a knowledge of the particular form of the probability density functions. However, such knowledge would be very useful for analysis of measured data which is always based on some limited number of samples (stirrer positions).

The starting point for deriving electric-field probability density functions is to write the rectangular components in terms of their real and imaginary parts:

$$E_x = E_{xr} + iE_{xi}, \quad E_y = E_{yr} + iE_{yi}, \quad E_z = E_{zr} + iE_{zi}. \tag{70}$$

(The dependence on $\boldsymbol{r}$ will be omitted where convenient because all of the results in this section are independent of $\boldsymbol{r}$.) The mean value of all the real and imaginary part in eq (70) is zero, as shown in eq (36):

$$<E_{xr}>=<E_{xi}>=<E_{yr}>=<E_{yi}>=<E_{zr}>=<E_{zi}>=0. \tag{71}$$

The variance of the real and imaginary parts can be shown to equal half the result for the complex components in eq (40):

$$<E_{xr}^2>=<E_{xi}^2>=<E_{yr}^2>=<E_{yi}^2>=<E_{zr}^2>=<E_{zi}^2>=\frac{E_0^2}{6}\equiv\sigma^2. \tag{72}$$

The mean and variance of the real and imaginary parts in eqs (71) and (72) are all the information that can be derived from the initial statistical assumptions in eqs (31) and (33).

However, the maximum entropy method [41],[42] can be used to derive the probability density functions from eqs (71) and (72). For example, consider E_{xr}. The maximum entropy method selects the probability density function $f(E_{xr})$ to maximize the entropy (uncertainty) given by the integral

$$-\int_{-\infty}^{\infty} f(E_{xr}) \ln[f(E_{xr})]\, dE_{xr} \tag{73}$$

subject to the constraints in eqs (71) and (73) and the usual probability constraint,

$$\int_{-\infty}^{\infty} f(E_{xr})\, dE_{xr} = 1. \tag{74}$$

The maximization of eq (73) subject to the constraints in eqs (71), (72), and (74) is performed by the method of Lagrange multipliers [42], and the result for f is the normal distribution:

$$f(E_{xr}) = \frac{1}{\sqrt{2\pi}\sigma} \exp\left[-\frac{E_{xr}^2}{2\sigma^2}\right], \tag{75}$$

where σ is defined in eq (72). The same probability density function also applies to the other real and imaginary parts of the electric field components. Even though there are other probability density functions that would satisfy the constraints in eqs (71), (72), and (74), the normal distribution in eq (75) maximizes the entropy given by eq (73) and is the least biased. Any other probability density function would have to be based on additional information that is not provided by this analysis.

Equations (27), (33), and (34) can be used to show that the real and imaginary parts of the electric-field components are uncorrelated. Only the derivation for $<E_{xr}E_{xi}>$ will be shown, but the derivations for the other correlations are similar. From eqs (27)-(31), the real and imaginary parts of E_x can be written:

$$\begin{aligned} E_{xr}(\boldsymbol{r}) = \iint_{4\pi} \{&[\cos\alpha\cos\beta\, F_{\alpha r}(\Omega) - \sin\beta\, F_{\beta r}(\Omega)]\cos(\boldsymbol{k}\bullet\boldsymbol{r}) \\ &- [\cos\alpha\cos\beta\, F_{\alpha i}(\Omega) - \sin\beta\, F_{\beta i}(\Omega)]\sin(\boldsymbol{k}\bullet\boldsymbol{r})\}\, d\Omega, \end{aligned} \tag{76}$$

$$\begin{aligned} E_{xi}(\boldsymbol{r}) = \iint_{4\pi} \{&[\cos\alpha\cos\beta\, F_{\alpha i}(\Omega) - \sin\beta\, F_{\beta i}(\Omega)]\cos(\boldsymbol{k}\bullet\boldsymbol{r}) \\ &+ [\cos\alpha\cos\beta\, F_{\alpha r}(\Omega) - \sin\beta\, F_{\beta r}(\Omega)]\sin(\boldsymbol{k}\bullet\boldsymbol{r})\}\, d\Omega. \end{aligned} \tag{77}$$

The average value of the product of eqs (76) and (77) can be evaluated by using eqs (32) and (33) inside the double integral and making use of the delta function to evaluate one integration. Then the remaining integrand is zero:

$$\begin{aligned} <E_{xr}(\boldsymbol{r})E_{xi}(\boldsymbol{r})> = \frac{E_0^2}{16\pi}\iint_{4\pi} &[\cos^2\alpha_2\cos^2\beta_2 + \sin^2\beta_2][\cos(\boldsymbol{k}_2\bullet\boldsymbol{r})\sin(\boldsymbol{k}_2\bullet\boldsymbol{r}) \\ &- \cos(\boldsymbol{k}_2\bullet\boldsymbol{r})\sin(\boldsymbol{k}_2\bullet\boldsymbol{r})]d\Omega = 0. \end{aligned} \tag{78}$$

Similar evaluations show that the real and imaginary parts of all three rectangular components are uncorrelated. Since they are Gaussian, they are also independent [43].

Since the real and imaginary parts of the rectangular components of the electric field have been shown to be normally distributed with zero mean and equal variances and are independent, the probability density functions of various electric field magnitudes or squared magnitudes are chi or chi-square distributions with the appropriate number of degrees of freedom. The magnitude of any of the electric field components, for example $|E_x|$, is chi distributed with two degrees of freedom and consequently has a Rayleigh distribution [43]:

$$f(|E_x|) = \frac{|E_x|}{\sigma^2}\exp\left[-\frac{|E_x|^2}{2\sigma^2}\right]. \tag{79}$$

Figure 10 shows a comparison of eq (79) with measured data taken at 1 GHz in the NASA A Chamber [8]. The chamber has two stirrers, and the total number of samples (stirrer positions) is 225. The data were taken with a small electric-field probe that was calibrated at NIST [8]. The agreement is about as good as can be expected with 225 samples.

The squared magnitude of any of the electric field components, for example $|E_x|^2$, is chi-square distributed with two degrees of freedom, and consequently it has an exponential distribution [44]:

$$f(|E_x|^2) = \frac{1}{2\sigma^2}\exp\left[-\frac{|E_x|^2}{2\sigma^2}\right]. \tag{80}$$

The probability density functions in eqs (79) and (80) agree with Kostas and Boverie [33]. They suggest that the exponential distribution in eq (80) is also applicable to the power received by a small, linearly polarized antenna, but it will shown later that the exponential distribution applies to the power received by any type of antenna.

The total electric field magnitude $|\boldsymbol{E}|$ is chi distributed with 6 degrees of freedom and has the following probability density function [33],[43]:

$$f(|\boldsymbol{E}|) = \frac{|\boldsymbol{E}|^5}{8\sigma^6}\exp\left[-\frac{|\boldsymbol{E}|^2}{2\sigma^2}\right]. \tag{81}$$

Figure 11 shows a comparison of eq (81) with measured data taken under the same conditions as in figure 10. In this case a three-axis, electric-field probe was used to take the data [8]. Again the agreement is about as good as can be expected for 225 samples.

The squared magnitude of the total electric field is chi-square distributed with 6 degrees of freedom and has the following probability density function [43]:

$$f(|\boldsymbol{E}|^2) = \frac{|\boldsymbol{E}|^4}{16\sigma^6}\exp\left[-\frac{|\boldsymbol{E}|^2}{2\sigma^2}\right]. \tag{82}$$

The dual probability density functions for the magnetic field can be obtained by starting with the variance of the real or imaginary parts of one of the magnetic field components, for example H_{xr}:

$$< H_{xr} >= \frac{E_0^2}{6\eta_0^2} \equiv \sigma_H^2 . \tag{83}$$

Then the dual of the results in eqs (79) through (82) can be obtained by replacing E by H and σ by σ_H.

Similar techniques can be used to analyze the signal received by an antenna. Equation (61) shows that the real and imaginary parts of the current, I_r and I_i, have zero mean:

$$< I_r >=< I_i >= 0. \tag{84}$$

The derivation of eq (66) can be modified to obtain the variance of the real and imaginary parts of the current:

$$< I_r^2 >=< I_i^2 >= \frac{1}{4R_r} \frac{E_0^2}{\eta} \frac{\lambda^2}{4\pi} \equiv \sigma_I^2 . \tag{85}$$

Since only the mean and variance of the the real and imaginary parts of the current are known, the maximum entropy method is again applicable for determining the probability density function. The result is again the normal distribution for both I_r and I_i:

$$f(I_r) = \frac{1}{\sqrt{2\pi}\sigma_I} \exp\left[-\frac{I_r^2}{2\sigma_I^2} \right] \quad \text{and} \quad f(I_i) = \frac{1}{\sqrt{2\pi}\sigma_I} \exp\left[-\frac{I_i^2}{2\sigma_I^2} \right]. \tag{86}$$

Equations (32), (33), (59), and (60) can be used to show that I_r and I_i are uncorrelated:

$$< I_r I_i >= 0. \tag{87}$$

Equations (84) through (87) can be used to show that the current magnitude $|I|$ is chi distributed with two degrees of freedom (Rayleigh distribution):

$$f(|I|) = \frac{|I|}{\sigma_I^2} \exp\left[-\frac{|I|^2}{2\sigma_I^2} \right]. \tag{88}$$

The current magnitude squared $|I|^2$ is chi-square distributed with two degrees of freedom (exponential distribution):

$$f(|I|^2) = \frac{1}{2\sigma_I^2} \exp\left[-\frac{|I|^2}{2\sigma_I^2} \right]. \tag{89}$$

From eq (62), the received power P_r is proportional to $I_r^2 + I_i^2$. So P_r is also chi-square distributed with two degrees of freedom and has an exponential probability density function:

$$f(P_r) = \frac{1}{2\sigma_I^2 R_r} \exp\left[-\frac{P_r}{2\sigma_I^2 R_r} \right]. \tag{90}$$

If the load is not matched, then the radiation resistance R_r in eq (90) is replaced by the load resistance R_l and the expression for σ_I^2 is modified from that given in eq (85). The result in eq (90) is in agreement with that of Kostas and Boverie [33], but its derivation is more general. It does not rely on the received power being proportional to the field at a point (such as an electric or magnetic field probe) and is valid for general extended antennas. The same result is applicable for general test objects as long as they are linear and have identifiable terminals with linear loads.

The result in eq (90) matches experimental data in reverberation chambers fairly well for a variety of antennas (dipoles, horns, and log-periodic dipole arrays). Figure 12 shows a comparison of eq (90) with data taken with a log-periodic dipole array at 1GHz in the NASA A Chamber [8]. The agreement is somewhat better than in figures 10 and 11 because the number of samples was increased to 1024. In figures 10 through 12, the transmitting antenna was a log-periodic dipole array.

3.4 Loss Mechanisms and Cavity Q

In eq (39), E_0^2 was introduced as the mean-square value of the electric field which was shown to be independent of position. This constant can be related to the power P_t transmitted and the chamber Q by conservation of power [5],[44]. The starting equation is the definition of quality factor (Q):

$$Q = \frac{\omega U}{P_d}, \tag{91}$$

where U is the energy stored in the cavity and P_d is the power dissipated. Since the average energy density was shown to be independent of position in eq (47), the stored energy can be written as the product of the average energy density and the chamber volume V:

$$U = < W > V. \tag{92}$$

For steady-state conditions, conservation of power requires that the dissipated power P_d equals the transmitted power P_t. Then eqs (47), (91), and (92) can be used to derive

$$E_0^2 = \frac{QP_t}{\omega \varepsilon V}. \tag{93}$$

This analysis can be carried further to relate the transmitted power to the power received by a receiving antenna located in the chamber. If eq (93) is substituted into eq (66), the average power received by a matched, lossless antenna is found to be

$$< P_r >= \frac{\lambda^3 Q}{16\pi^2 V} P_t . \tag{94}$$

Equations (93) and (94) show the importance of the Q enhancement in determining the field strength or the received power in the chamber. The most popular method of measuring Q is based on the solution of eq (94) for Q:

$$Q = \frac{16\pi^2 V}{\lambda^3} \frac{< P_r >}{P_t} . \tag{95}$$

Equation (95) is applicable to an impedance-matched, lossless receiving antenna, but dissipative or mismatch losses can be accounted by modifying the effective area as shown in eq (68).

The calculation of chamber Q requires that all losses are accounted in evaluating P_d in eq (91). A theory has been developed for including the following four types of loss [5]:

$$P_d = P_{d1} + P_{d2} + P_{d3} + P_{d4} , \tag{96}$$

where P_{d1} is the power dissipated in the cavity walls, P_{d2} is the power absorbed in loading objects within the cavity, P_{d3} is the power lost through aperture leakage, and P_{d4} is the power dissipated in the loads of receiving antennas. By substituting eq (96) into eq (91), we can write the following expression for the inverse of Q:

$$Q^{-1} = Q_1^{-1} + Q_2^{-1} + Q_3^{-1} + Q_4^{-1} , \tag{97}$$

where

$$Q_1 = \frac{\omega U}{P_{d1}}, Q_2 = \frac{\omega U}{P_{d2}}, Q_3 = \frac{\omega U}{P_{d3}}, \text{ and } Q_4 = \frac{\omega U}{P_{d4}} . \tag{98}$$

The four loss mechanisms can be analyzed as follows. Wall loss is usually dominant, so it will be covered in most detail.

For highly conducting walls, the plane-wave integral representation can be analytically continued all the way to the wall surfaces, and the reflected fields are related to the incident fields via plane-wave reflection coefficients as shown in figure 13. Then P_{d1} in eq (98) can be evaluated in terms of the wall area A and the wall reflection coefficient. The resultant expression to be evaluated for Q_1 is [45]

$$Q_1 = \frac{2kV}{A < (1 - |\Gamma|^2) \cos\theta >_\Omega} , \tag{99}$$

where $< >_\Omega$ indicates an average over incidence angle and polarization and Γ is a reflection coefficient.

The reflection coefficients for TE (perpendicular) polarization Γ_{TE} and TM (parallel) polarization Γ_{TM} are given by [26]

$$\Gamma_{TE} = \frac{\mu_w k \cos\theta - \mu\sqrt{k_w^2 - k^2 \sin^2\theta}}{\mu_w k \cos\theta + \mu\sqrt{k_w^2 - k^2 \sin^2\theta}} \tag{100}$$

and

$$\Gamma_{TM} = \frac{\mu k_w^2 \cos\theta - \mu_w k\sqrt{k_w^2 - k^2 \sin^2\theta}}{\mu k_w^2 \cos\theta + \mu_w k\sqrt{k_w^2 - k^2 \sin^2\theta}}, \tag{101}$$

where $k_w = \omega\sqrt{\mu_w(\varepsilon_w + i\sigma_w/\omega)}$, σ_w is the wall conductivity, ε_w is the wall permittivity, and μ_w is the wall permeability. To account equally for both polarizations in eq (99), the average quantity can be written

$$\begin{aligned} <(1-|\Gamma|^2)\cos\theta>_\Omega &= <[1-\frac{1}{2}(|\Gamma_{TE}|^2 + |\Gamma_{TM}|^2)]\cos\theta>_\Omega \\ &= \int_0^{\pi/2}[1-\frac{1}{2}(|\Gamma_{TE}|^2 + |\Gamma_{TM}|^2)]\cos\theta\sin\theta\,d\theta. \end{aligned} \tag{102}$$

For $|k_w/k| >> 1$, the squares of the reflection coefficients can be approximated

$$|\Gamma_{TE}|^2 \approx 1 - \frac{4\mu_w k\,\mathrm{Re}(k_w)\cos\theta}{\mu|k_w|^2} \tag{103}$$

and

$$|\Gamma_{TM}|^2 \approx 1 - \frac{4\mu_w k\,\mathrm{Re}(k_w)}{\mu|k_w|^2\cos\theta}, \tag{104}$$

where Re indicates real part. Substitution of eqs (102) through (104) into eq (99) yields

$$Q_1 \approx \frac{3|k_w|^2 V}{4A\mu_r\,\mathrm{Re}(k_w)}, \tag{105}$$

where $\mu_r = \mu_w/\mu$.

Equation (105) does not require that the walls be highly conducting. However, if the walls are highly conducting and $\sigma_w/(\omega\varepsilon_w) >> 1$, then Q_1 simplifies to

$$Q_1 \approx \frac{3V}{2\mu_r \delta A}, \tag{106}$$

where $\delta \approx 2/\sqrt{\omega\mu_w\sigma_w}$. This is the usual expression for reverberation chamber Q for the case where wall losses are dominant. A related derivation has employed the skin depth approximation from the start followed by an average over an ensemble of plane waves [3]. For the case of a rectangular cavity where the modes are known, it has been derived by averaging the modal Q values for modes whose resonant frequencies are in the vicinity of the excitation frequency [18]. The modal derivation for rectangular cavities was done for the case $\mu_r = 1$, and a correction was derived for rectangular cavities [18]. The correction is important only at low frequencies.

If the cavity contains absorbers (lossy objects distinct from the walls), the absorption loss P_{d2} can be written in terms of the absorption cross section σ_a [46] which is generally a function of incidence angle and polarization:

$$P_{d2} = S < \sigma_a >_\Omega . \tag{107}$$

The appropriate average is over 4π steradians and both (TE and TM) polarizations [44]:

$$< \sigma_a >_\Omega = \frac{1}{8\pi} \iint_{4\pi} (\sigma_{aTE} + \sigma_{aTM})\, d\Omega. \tag{108}$$

The absorption cross section in eq (108) can be that of a single object or a summation for multiple absorbers. For example, for M absorbers $< \sigma_a >_\Omega$ is replaced by

$$< \sigma_a >_\Omega = \sum_{i=1}^{M} < \sigma_{ai} >_\Omega , \tag{109}$$

where $< \sigma_{ai} >$ is the averaged absorption cross section of the ith absorber. From eqs (98) and (107) the result for Q_2 is [44]

$$Q_2 = \frac{2\pi V}{\lambda < \sigma_a >_\Omega}. \tag{110}$$

The formulation for leakage loss P_{d3} is similar to that of absorption loss because apertures can be characterized by a transmission cross section σ_l [47]. However, only plane waves that propagate toward the wall aperture(s) contribute to leakage power. So the expression for Q_3 is modified from eq (110) by a factor of 2 [44]:

$$Q_3 = \frac{4\pi V}{\lambda < \sigma_l >_\Omega}. \tag{111}$$

Also, the angular average is over 2π steradians ($0 \le \theta \le \pi/2$):

$$< \sigma_l >_\Omega = \frac{1}{4\pi} \iint_{2\pi} (\sigma_{l\mathrm{TE}} + \sigma_{l\mathrm{TM}})\, d\Omega. \tag{112}$$

For the case of L apertures, $< \sigma_l >_\Omega$ in eq (112) is replaced by a summation:

$$< \sigma_l >_\Omega = \sum_{i=1}^{L} < \sigma_{li} >_\Omega, \tag{113}$$

where $< \sigma_{li} >_\Omega$ is the averaged transmission cross section of the ith aperture. For electrically large apertures, $< \sigma_l >_\Omega$ is independent of frequency and Q_3 is proportional to frequency. For small or resonant apertures, the frequency dependence of Q_3 is more complicated. The Q of a cavity with a circular aperture has been studied theoretically and experimentally [44].

The power dissipated in the load of a receiving antenna is covered in Section 3.2. For a lossless receiving antenna, P_{d4} can be written

$$P_{d4} = \frac{m\lambda^2}{8\pi} S, \tag{114}$$

where m is the impedance mismatch. From eqs (98) and (114), Q_4 can be written

$$Q_4 = \frac{16\pi^2 V}{m\lambda^3}. \tag{115}$$

If there are multiple receiving antennas, eqs (114) and (115) can be modified accordingly. For example, if there are N identical receiving antennas, P_{d4} is multiplied by N and Q_4 is divided by N. For a matched load (m =1), Q_4 is proportional to frequency cubed. This means that Q_4 is small for low frequencies and is the dominant contributor to the total Q in eq (97). The effect of antenna loading on the Q of reverberation chambers has been observed experimentally [11]. At high frequencies, Q_4 becomes large and contributes little to the total Q.

A comparison of measured and calculated Q [44] is shown in figure 14 for a rectangular aluminum cavity of dimensions 0.514 m × 0.629 m × 1.75 m. The Q measurements were performed by the power ratio method of eq (95) and decay time method as discussed in Appendix D. Standard-gain, K_u-band horn antennas were used to cover the frequency range from 12 to 18 GHz. The measured Q values fall below the theoretical Q, but the agreement is much better than that obtained in earlier comparisons [2]. The decay-time measurement [7] generally agrees better than the power-ratio method because it is less affected by antenna efficiency and impedance mismatch.

A second comparison of theory and measurement in figure 15 shows the effect of loading the cavity with three spheres of radius 0.066 m filled with salt water [44]. In this case the absorption loss as described by eq (110) decreases the Q dramatically. Broadband ridged horns were used for the Q measurements, and the agreement with theory is not as good. However, the decay-time measurement is again a significant improvement over the power-ratio measurment.

4. RADIATED EMISSIONS

Reverberation chambers have been used primarily for radiated immunity measurements, and as a result a great deal of research has been done in characterizing chamber fields. However, reverberation chambers are reciprocal devices, and they can and have been used for radiated emissions measurements [39]. The quantity measured is the total radiated power, and the measurement can be explained by either power conservation [44] or reciprocity [48].

4.1 Radiated Power

If the equipment under test (EUT) radiates (transmits) power P_{tEUT}, eq (94) can be used to determine the average power $<P_{rEUT}>$ received by a matched, lossless reference antenna. Equation (94) is based on conservation of power, and it can be solved for P_{tEUT}:

$$P_{tEUT} = \frac{16\pi^2 V}{\lambda^3 Q} < P_{rEUT} > . \tag{116}$$

In theory this equation could be used directly for measurement of P_{tEUT}. However, eq (116) requires that the chamber volume V and (loaded) Q be known. It also requires that the receiving antenna be impedance matched and lossless or that the received power be corrected for antenna effects.

A better way to determine P_{tEUT} is to perform a separate reference measurement under the same chamber conditions. If a known power P_{tref} is transmitted and an average power $<P_{rref}>$ is received, the coefficient on the right side of eq (116) can be determined:

$$\frac{16\pi^2 V}{\lambda^3 Q} = \frac{P_{tref}}{< P_{rref} >} . \tag{117}$$

Then P_{tEUT} can be determined by the ratio

$$P_{tEUT} = \frac{P_{tref}}{< P_{rref} >} < P_{rEUT} > . \tag{118}$$

If the same receiving antenna is used for both the EUT and the reference measurement, this method has the additional advantage of approximately canceling efficiency and impedance mismatch effects of the receiving antenna.

This was done in the measurement of radiated power from a microstrip line [40], and the agreement between theory and measurement as shown in figure 16 was good. The actual quantity plotted was the following power ratio

$$\frac{< P_{rref} >}{< P_{rEUT} >} = \frac{P_{tref}}{P_{rEUT}}. \tag{119}$$

Since the same input power was fed to the reference antenna and the microstrip line, the ratio in figure 16 can be interpreted as either a shielding effectiveness or the reciprocal of the radiation efficiency of the microstrip line.

4.2 Reciprocity Relationship to Radiated Immunity

Electromagnetic reciprocity has many mathematical forms, and it can be applied to fields, circuits, or a mixture of the two [49]. Since reciprocity involves interchanging the source and receiver, it provides a method for relating radiated emissions and immunity. Consider an EUT located at the center of a spherical volume as shown in figure 17. In an immunity measurement, the EUT is illuminated by incident electric and magnetic fields, $\boldsymbol{E}_i$ and $\boldsymbol{H}_i$, due to sources located outside the spherical surface S_r. In an emissions measurement, the EUT radiates (transmits) electric and magnetic fields, $\boldsymbol{E}_t$ and $\boldsymbol{H}_t$.

A typical EUT is very complex, and de Hoop and Quak [48] have developed a multi-port reciprocity formulation to relate emissions and immunity. Here we consider the simpler special case of a single port within the EUT as shown in figure 18. In an immunity measurement the incident fields induce an open-circuit voltage V_i, and Z_t is the impedance of the Thevenin equivalent circuit. An arbitrary load impedance Z_l is connected across the terminals. In an emissions measurement, V_i is zero and a current I_t flows in the loop. The radiated fields are proportional to I_t and can be normalized as follows:

$$\boldsymbol{E}_t(\boldsymbol{r}) = I_t \boldsymbol{e}_n(\boldsymbol{r}) \quad \text{and} \quad \boldsymbol{H}_t(\boldsymbol{r}) = I_t \boldsymbol{h}_n(\boldsymbol{r}), \tag{120}$$

where $\boldsymbol{e}_n$ and $\boldsymbol{h}_n$ are the electric and magnetic fields that are radiated when $I_t = 1$ A. If reciprocity is applied at the circuit terminals and the spherical surface, the following expression is obtained for V_i [48],[50]:

$$V_i = -\iint_{S_r} \hat{\boldsymbol{r}} \bullet [\boldsymbol{e}_n(\boldsymbol{r}) \times \boldsymbol{H}_i(\boldsymbol{r}) - \boldsymbol{E}_i(\boldsymbol{r}) \times \boldsymbol{h}_n(\boldsymbol{r})] \mathrm{d}S_r. \tag{121}$$

Up to this point, eq (121) is fairly general because there are no restrictions on the sphere radius r or the incident fields. If the surface integral in eq (121) is performed in the far field of the EUT ($kr >> 1$), the normalized EUT fields can be written in the following forms

$$e_n(r) = e_t(\theta,\phi)\frac{\exp(ikr)}{r},$$

$$h_n(r) = \hat{r} \times e_t(\theta,\phi)\frac{\exp(ikr)}{\eta r}, \tag{122}$$

where $e_t(\theta,\phi) \bullet \hat{r} = 0$ and θ and ϕ are standard spherical coordinates. To apply eq (121) to reverberation chamber measurements, the incident electric and magnetic fields are replaced by plane-wave integral representations from eqs (27) and (41). Then eq (121) can be rewritten as

$$\begin{aligned} V_i = -\iint_{S_r} \frac{\exp(ikr)}{r}\hat{r} \bullet \{e_t(\theta,\phi) \times [\frac{1}{\eta}\iint_{4\pi} \hat{k} \times F(\Omega)\exp(ik \bullet r)\,\mathrm{d}\Omega] \\ -[\iint_{4\pi} F(\Omega)\exp(ik \bullet r)\,\mathrm{d}\Omega] \times [\frac{1}{\eta}\hat{r} \times e_t(\theta,\phi)]\}\,\mathrm{d}S_r. \end{aligned} \tag{123}$$

To evaluate the surface integration, it is written explicitly in terms of spherical coordinates:

$$\iint_{S_r}\{\quad\}\,\mathrm{d}S_r = \int_0^{2\pi}\int_0^{\pi}\{\quad\}r^2\sin\theta\,\mathrm{d}\theta\,\mathrm{d}\phi. \tag{124}$$

The exponential factor $\exp(ik \bullet r)$ in eq (123) is a rapidly oscillating function of θ and ϕ except at the stationary point $\hat{r} = -\hat{k}$. A stationary-phase [51] evaluation of eq (123) yields

$$\begin{aligned} V_i = \frac{2\pi i}{k\eta}\iint_{4\pi} \hat{k} \bullet \{e_t(\alpha,\beta) \times [\hat{k} \times F(\Omega)] \\ + F(\Omega) \times [\hat{k} \times e_t(\alpha,\beta)]\}\,\mathrm{d}\Omega. \end{aligned} \tag{125}$$

Because the reciprocity integral in eq (121) is independent of the surface over which it is evaluated, the result in eq (125) is an exact, rather than an asymptotic, result. (This is consistent with the observation that eq (125) is independent of r.) Vector identities can be used to reduce eq (125) to

$$V_i = \frac{4\pi i}{k\eta}\iint_{4\pi} e_t(\alpha,\beta) \bullet F(\Omega)\,\mathrm{d}\Omega. \tag{126}$$

This is as far as the expression for V_i can be simplified. It shows that the open-circuit voltage induced when the EUT is illuminated in an immunity test is proportional to a weighted integral of the transmitted far field e_t when the EUT is transmitting. Equation (126) is similar to the earlier receiving response in eq (59) except that the receiving function in eq (59) was not

derived in terms of the transmission properties of the antenna. Another interpretation of eq (126) is that the transmitting and receiving patterns of an antenna or an EUT are the same.

The statistical properties of the plane-wave spectrum $F(\Omega)$ were discussed in Section 3.1, and they can be used to derive the statistical properties of V_i. For example, eqs (31) and (126) can be used to show that the average value of V_i is zero:

$$< V_i >= \frac{4\pi i}{k\eta} \iint_{4\pi} e_t(\alpha,\beta) \bullet < F(\Omega) > \mathrm{d}\Omega = 0. \tag{127}$$

The mean square value of V_i is the most useful quantity because it is proportional to the received power in an emissions measurement. The squared magnitude $|V_i|^2$ can be written

$$|V_i|^2 = \left(\frac{4\pi}{k\eta}\right)^2 \iint_{4\pi}\iint_{4\pi} [e_t(\alpha_1,\beta_1) \bullet F(\Omega_1)][e_t^*(\alpha_2,\beta_2) \bullet F^*(\Omega_2)]\,\mathrm{d}\Omega_1\,\mathrm{d}\Omega_2\,. \tag{128}$$

The average value $<|V_i|^2>$ can be determined by applying the properties of F in eqs (34) and (35) to eq (128):

$$<|V_i|^2> = \frac{2\pi E_0^2}{k^2\eta^2} \iint_{4\pi} |e_t(\alpha_1,\beta_1)|^2\,\mathrm{d}\Omega_1\,. \tag{129}$$

From eq (122), the integral on the right side of eq (129) can be related to the total radiated power P_{rad1} when a current of 1 A is flowing in the circuit in figure 14:

$$P_{rad1} = \frac{r^2}{\eta} \iint_{4\pi} |e_n(\alpha,\beta)|^2\,\mathrm{d}\Omega = \frac{1}{\eta} \iint_{4\pi} |e_t(\alpha,\beta)|^2\,\mathrm{d}\Omega. \tag{130}$$

Substitution of eq (130) into eq (129) yields

$$<|V_i|^2> = \frac{2\pi E_0^2}{k^2\eta} P_{rad1}\,. \tag{131}$$

Equation (131) shows that the total radiated power in an emissions measurement is proportional to the mean-square, induced voltage in an immunity measurement. For an arbitrary current I in the transmitting (emissions) case, the radiated power P_{rad} is given by

$$P_{rad} = |I|^2\, R_{rad}\,, \tag{132}$$

where R_{rad} is the radiation resistance part of the transmitting impedance Z_t in figure 18. For $I = 1\mathrm{A}$, we have $P_{rad1} = R_{rad}$. If we substitute for P_{rad1} and k ($= 2\pi/\lambda$), eq (131) can be rewritten

$$\frac{<|V_i|^2>/(4R_{rad})}{E_0^2/\eta} = \frac{\lambda^2}{8\pi}. \tag{133}$$

The numerator of the left side of eq (133) is the received power for the case of a matched load $(Z_L = Z_t^*)$ with no dissipative loss in the circuit $(\mathrm{Re}(Z_t) = R_{rad})$ in figure 18, and the denominator is the scalar power density. This ratio is the average effective area, and it is equal to $\lambda^2/8\pi$ as shown previously in eq (66).

If the circuit in figure 18 has loss $(\mathrm{Re}(Z_t) = R_{rad} + R_{loss})$ but is still impedance matched $(Z_L = Z_t^*)$, eq (133) can be manipulated to the following form

$$\frac{\{<|V_i|^2>/[4(R_{rad} + R_{loss})]\}/\{E_0^2/\eta\}}{\lambda^2/8\pi} = \frac{R_{rad}}{R_{rad} + R_{loss}}. \tag{134}$$

In eq (134), the numerator is the average received power divided by the scalar power density which equals the average effective area. The denominator $\lambda^2/8\pi$ is the maximum effective area for any receiving antenna in a well-stirred field. Kraus [52] has termed this ratio "effectiveness ratio, α_i" for the simpler case where the incident is a plane wave which can be polarization matched by the receiving antenna to yield a maximum effective area of $\lambda^2/4\pi$. The right side of eq (134) is the radiation efficiency η_a for the emissions case. So we can rewrite eq (134):

$$\alpha_i \text{ (immunity)} = \eta_a \text{ (emissions)}. \tag{135}$$

The theoretical and experimental results in figures 9 and 16 provide a verification of eq (135) for the specific case of a microstrip transmission line. Typically in the EMC community the left side of eq (135) is called shielding effectiveness and is given in decibels. If there is impedance mismatch, both sides of eq (134) can be multiplied by the same mismatch factor to provide a comparison with ideal receivers or transmitters.

5. CONCLUSIONS AND RECOMMENDATIONS

As a result of the complexity of reverberation chambers, a number of theoretical methods are needed to provide an electromagnetic characterization. Mode theory is usually the method of choice for cavity analysis, and it has been useful for determining mode density and modal and composite Q for rectangular cavities [18]. However, it is not convenient for quantitative analysis of real chambers with mechanical stirring because the cavity modes are hard to determine and they change with stirrer rotation. Ray theory can provide some useful insight, but it is also difficult to use for real, high-Q chambers because of the geometrical complexity and the slow convergence of ray sums.

A plane-wave, integral representation with a statistically uniform angular spectrum is useful for describing well-stirred fields. It has the advantage of being easy to use for describing antenna and test-object responses because it uses only propagating plane waves. It is most directly useful for predicting results in immunity measurements as in Section 3, but reciprocity can be used to predict results in emissions measurements as in Section 4. When the maximum

entropy method is applied to the results of the integral representation, probability density functions can be derived for many field and antenna response quantities. These statistical results are in agreement with other statistical theories that are based on the central limit theorem and with experimental results.

A number of theoretical extensions and improvements would be useful. For deterministic field calculations, modern computational tools could be used to characterize chamber fields and the effectiveness of mechanical stirring. The transmission line method (TLM) has been used to study a simple two-dimensional model of mechanical stirring [24], and the finite element method has been used for three-dimensional analysis of chambers [53]. The use of the rectangular cavity Green's function in an efficient form [19] has been suggested for method-of-moments analysis of mechanical stirring. Numerical methods are most likely to be successful at lower frequencies where the electrical size of the cavity is not too large, and this is an important frequency range where real chambers have operational problems (such as ineffective stirring, poor field uniformity, and antenna impedance mismatch). A long-standing question regarding mechanical stirring is how much frequency shift of a given mode can be generated by stirrer rotation so that a meaningful comparison with frequency stirring [11],[12] can be made.

Some extensions in the plane-wave, integral representation would also be useful. The theory is most applicable to ensemble averages, but most immunity testing uses peak values rather than average values. For a finite number of samples, the probability density functions in section 3.3 can be used to predict peak values, and this has worked fairly well for modest numbers of samples. However, these peak values approach infinity as the number of samples approaches infinity. For quantities such as received power, this is not physically possible. The plane-wave, integral representation can probably still be used, but the tails of the distribution need some modification to satisfy energy conservation. Another idealization that requires some further attention is the delta function for angular correlation in eq (33). For real, imperfect stirring, the delta function probably needs to be replaced by a peaked function with nonzero width. A final point that requires further study is the region of validity of the plane-wave, integral representation for the electric field in eq (27). Even though this expression gives good results when analytically continued outside a spherical, source-free region [39],[45], the validity of this analytical continuation has not been rigorously demonstrated. This question has practical consequences for field uniformity, stirring, and testing since rectangular test volumes are often used in practice.

This research was partially supported by the American Automobile Manufacturers Association (AAMA). I thank John Ladbury for providing figures 10 through 12 and for making a number of useful suggestions on the manuscript.

REFERENCES

[1] Mendes, H.A. A new approach to electromagnetic field-strength measurements in shielded enclosures. Wescon, Los Angeles, CA; 1968.

[2] Crawford, M.L.; Koepke, G.H. Design, evaluation, and use of a reverberation chamber for performing electromagnetic susceptibility/vulnerability measurements. Nat. Bur. Stand. (U.S.) Technical Note 1092; 1986.

[3] Dunn., J.M. Local, high-frequency analysis of the fields in a mode-stirred chamber. *IEEE Trans. Electromagn. Compat., 32*: 53-58; 1990.

[4] Lehman, T.H. A statistical theory of electromagnetic fields in complex cavities. EMP Interaction Note 494; May 1993.

[5] Hill, D.A.; Ma, M.T.; Ondrejka, A.R.; Riddle, B.F.; Crawford, M.L.; Johnk, R.T. Aperture excitation of electrically large, lossy cavities. *IEEE Trans. Electromagn. Compat., 36*: 169-177; 1994.

[6] Crawford, M.L.; Ma, M.T.; Ladbury, J.L.; Riddle, B.F. Measurement and evaluation of a TEM/reverberating chamber. Natl. Inst. Stand. Technol. Technical Note 1342; 1990.

[7] Ladbury, J.M.; Johnk, R.T.; Ondrejka, A.R. Rapid evaluation of mode-stirred chambers using impulsive waveforms. Natl. Inst. Stand. Technol. Technical Note 1381; 1996.

[8] Ladbury, J.M.; Koepke, G.H.; Camell, D.G. Evaluation of the NASA Langley Research Center mode-stirred chamber facility. Natl. Inst. Stand. Technol. Technical Note 1508; 1999.

[9] Ladbury, J.M. Statistical theory of reverberation chambers. Natl. Inst. Stand. Technol. Technical Note, in preparation.

[10] Koepke, G.H.; Ladbury, J.M.; Hill, D.A. The application of reverberation chambers to EMC testing. Natl. Inst. Stand. Technol. Technical Note, in preparation.

[11] Loughry, T.A. Frequency stirring: an alternate approach to mechanical mode-stirring for the conduct of electromagnetic susceptibility testing. Phillips Laboratory, Kirtland Air Force Base, NM, Technical Report 91-1036; 1991.

[12] Hill, D.A. Electronic mode stirring for reverberation chambers. *IEEE Trans. Electromagn. Compat., 36*: 294-299; 1994.

[13] Hill, D.A. Plane-wave, integral representation for fields in reverberation chambers. *IEEE Trans. Electromagn. Compat., 40*: 209-217; 1998.

[14] Borgnis, F.E.; Pappas, C.H. Electromagnetic waveguides and resonators. *Encyclopedia of Physics, Volume XVI, Electromagnetic Fields and Waves* (ed., S. Flugge), Berlin: Springer-Verlag; 1958.

[15] Ghose, R.N. *Microwave Circuit Theory and Analysis.* New York: McGraw-Hill Book Co.; 1963.

[16] Argence, E.; Kahan, T. *Theory of Waveguides and Cavity Resonators.* New York: Hart Publishing Co.; 1968.

[17] Huang, Y.; Edwards, D.J. An Investigation of electromagnetic field inside a moving wall mode-stirred chamber. IEE Conference on Electromagnetic Compatibility, Edinburgh, UK: 115-119; 1992.

[18] Liu, B.-H.; Chang, D.C.; Ma, M.T. Eigenmodes and the composite quality factor of a reverberating chamber. Nat. Bur. Stand. (U.S.) Technical Note 1066; 1983.

[19] Wu, D.I.; Chang, D.C. An investigation of a ray-mode representation of the Green's function in a rectangular cavity. Nat. Bur. Stand. (U.S.) Technical Note 1312; 1987.

[20] Harrington, R.F. *Time-Harmonic Electromagnetic Fields.* New York: McGraw-Hill; 1961.

[21] Smythe, W.R. *Static and Dynamic Electricity.* New York: McGraw-Hill; 1968.

[22] McDonald, S.W.; Kaufman, A.N. Wave chaos in the stadium: Statistical properties of short-wave solutions of the Helmholtz equation. *Phys. Rev. A, 37*: 3067-3086; 1988.

[23] Yaghjian, A.D. Electric dyadic Green's functions in the source region. *Proc. IEEE, 68*: 248-263; 1980.

[24] Wu, D.I.; Chang, D.C. The effect of an electrically large stirrer in a mode-stirred chamber. *IEEE Trans. Electromagn. Compat., 31*: 164-169; 1989.

[25] Huang, Y.; Edwards, D.J. A novel reverberating chamber: The source-stirred chamber. IEE Conference on Electromagnetic Compatibility, Edinburgh, UK: 120-124; 1992.

[26] Stratton, J.A. *Electromagnetic Theory.* New York: McGraw Hill; 1941.

[27] Wittmann, R.C.; Black, D.N. Quiet-zone evaluation using a spherical synthetic-aperture radar. IEEE Antennas and Propagation International Symposium, Montreal: 148-151; 1997.

[28] Hill, D.A. Spatial correlation function for fields in reverberation chambers. *IEEE Trans. Electromagn. Compat., 37*: 138; 1995.

[29] Zacharias, R.A.; Ng, N.C.; Lehman, T.H. Applying statistical electromagnetic theory to mode-stirred chamber measurements. Lawrence Livermore Nat. Lab. Rep. UCRL-ID-115667; 1993.

[30] Ishimaru, A. *Wave Propagation and Scattering in Random Media.* New York: Academic Press: 1978.

[31] Wolf, E. New theory of radiative energy transfer in free electromagnetic fields. *Phys. Rev. D, 13*: 869-886; 1976.

[32] Cook, R.K.; Waterhouse, R.V.; Berendt, R.D.; Edelman, S.; Thompson, M.C. Measurement of correlation coefficients in reverberant sound fields. *J. Acoust. Soc. Amer., 27*: 1072-1077; 1955.

[33] Kostas, J.G.; Boverie, B. Statistical model for a mode-stirred chamber. *IEEE Trans. Electromagn. Compat., 33*: 366-370; 1991.

[34] Kerns, D.M. *Plane-Wave Scattering Matrix Theory of Antennas and Antenna-Antenna Interactions.* Nat. Bur. Stand. (U.S.) Monograph 162; 1981.

[35] Park, P.K.; Tai, C.T. Receiving antennas. Ch. 6 in *Antenna Handbook* (ed., Y.T. Lo and S.W. Lee). New York: Van Nostrand Reinhold Co.; 1988.

[36] Tai, C.T. On the definition of effective aperture of antennas. *IEEE Trans. Antennas Propagat., 9*: 224-225; 1961.

[37] Corona, P.; Latmiral, G.; Paolini, E. Performance and analysis of a reverberating enclosure with variable geometry. *IEEE Trans. Electromagn. Compat., 22*: 2-5; 1980.

[38] Hill, D.A.; Camell, D.G.; Cavcey, K.H.; Koepke, G.H. Radiated emissions and immunity of microstrip transmission lines: Theory and reverberation chamber measurements. *IEEE Trans. Electromagn. Compat., 38*: 165-172; 1996.

[39] Hill, D.A.; Crawford, M.L.; Kanda, M.; Wu, D.I. Aperture coupling to a coaxial air line: Theory and experiment. *IEEE Trans. Electromagn. Compat., 35*: 69-74; 1993.

[40] Hill, D.A.; Camell, D.G.; Cavcey, K.H.; Koepke, G.H. Radiated emissions and immunity of microstrip transmission lines; Theory and measurements. Natl. Inst. Stand. Technol. Technical Note 1377; 1995.

[41] Baker-Jarvis, J.; Racine, M. Solving differential equations by a maximum entropy-minimum norm method with applications to Fokker-Planck equations. *J. Math. Phys., 30*: 1459-1453; 1989.

[42] Kapur, J.N.; Kesavan, H.K. *Entropy Optimization Principles with Applications.* Boston: Academic Press; 1992.

[43] Papoulis, A. *Probability, Random Variables, and Stochastic Processes.* New York: McGraw-Hill; 1965.

[44] Hill, D.A.; Adams, J.W.; Ma, M.T.; Ondrejka, A.R.; Riddle, B.F.; Crawford, M.L.; Johnk, R.T. Aperture excitation of electrically large, lossy cavities. Natl. Inst. Stand. Technol. Technical Note 1361; 1993.

[45] Hill, D.A. A reflection coefficient derivation for the Q of a reverberation chamber. *IEEE Trans. Electromagn. Compat., 38*: 591-592; 1996.

[46] Van de Hulst, H.C. *Light Scattering by Small Particles.* New York: Dover; 1981.

[47] Butler, C.M.; Rahmat-Samii, Y.; Mittra, R. Electromagnetic penetration through apertures in conducting surfaces. *IEEE Trans. Antennas Propagat., 26*: 82-93; 1978.

[48] De Hoop, A.T.; Quak, D. Maxwell fields and Kirchhoff circuits in electromagnetic interference. Technical University of Delft, Netherlands, Report Et/EM 1995-34; 1995.

[49] Monteath, G.D. *Applications of the Electromagnetic Reciprocity Principle.* Oxford: Pergamon Press; 1973.

[50] De Hoop, A.T. *Radiation and Scattering of Waves.* London: Academic Press; 1995.

[51] James, G.L. *Geometrical Theory of Diffraction for Electromagnetic Waves.* Stevenage, UK: Peter Perigrinus; 1976.

[52] Kraus, J.D. *Antennas.* New York: McGraw-Hill; 1950.

[53] Bunting, C.F.; Moeller, K.J.; Reddy, C.J. Finite element analysis of reverberation chambers. IEEE International Symposium on Electromagnetic Compatibility, Denver, CO; 1998.

[54] Hamid, M.A.K.; Johnson, W.A. Ray-optical solution for the dyadic Green's function in a rectangular cavity. *Electron. Lett., 6*: 317-319; 1970.

[55] Kwon, D.H.; Burkholder, R.J.; Pathak, P.H. Ray analysis of electromagnetic field build-up and quality factor of electrically large shielded enclosures. *IEEE Trans. Electromagn. Compat., 40*: 19-26; 1998.

[56] Richardson, R.E. Mode-stirred calibration factor, relaxation time, and scaling laws. *IEEE Trans. Instrum. Meas., 34*: 573-580; 1985.

APPENDIX A. RAY THEORY

The mathematical link between mode theory and ray theory for a perfectly conducting, rectangular cavity is the three-dimensional Poisson sum formula [19],[54]. This formula allows the Green's function in eq (15) to be converted from a triple sum of modes to a triple sum of rays. The mathematical details are fairly involved and will not be covered here. However, the physical interpretation is clearly pictured in terms of multiple images as shown in figure 19. The source is a z-directed dipole, and the multiple images represent multiple ray bounces in the $y = y'$ plane. Similar diagrams could be generated for other sources and locations.

The computation of the field at a point in the cavity is tedious because of the triple sum of image contributions. In fact the sum is not convergent for some frequencies and field locations. This has to be the case because the mode sum in eq (15) has infinities at resonant frequencies of each cavity mode. The mode representation is made finite for imperfectly conducting walls by introducing a finite Q (hence the resonant frequencies become complex). The ray sum can be made finite for imperfectly conducting walls by introducing a reflection coefficient (which has magnitude less than one) at each wall bounce. This has been done for studying the field buildup in a rectangular cavity when the source is a turned-on sinusoid [55].

Multiple-image theory can be extended to include the effect of a mechanical stirrer. Each image cell then contains an image of the mechanical stirrer with appropriate location and orientation as shown in figure 20. The solution of the large boundary value problem would be extremely difficult, even with the ray tracing approximation. However, the multiple-image diagram in figure 20 can be used to provide some insight into stirrer design. The goals of stirring are to randomize the field and to eliminate any deterministic component. Another way to state these goals is to minimize the ratio of unstirred to stirred energy. Unstirred energy arrives at the observation without interacting with the stirrer. An example is (single-bounce) ray U in figure 20. A stirring strategy then is to design the stirrer (or stirrers) to eliminate as many direct rays as possible. The conclusion that follows is that the stirrer(s) must be comparable to chamber size rather than just comparable to a wavelength. This conclusion is consistent with recent chamber measurements [8].

APPENDIX B. SHORT ELECTRIC DIPOLE

Consider a short electric dipole of effective length L oriented in the z direction as shown in figure 21. The components, $S_{r\alpha}$ and $S_{r\beta}$, of the dipole receiving function are given by

$$S_{r\alpha} = \frac{L \sin \alpha}{2R_r} \quad \text{and} \quad S_{r\beta} = 0, \tag{B1}$$

where R_r is the radiation resistance. In eq (B1), $S_{r\alpha}$ is derived by dividing the induced voltage by twice the radiation resistance for a matched load. If eq (B1) is substituted into eq (63), the angular integration can be carried out to obtain

$$< P_r > = \frac{E_0^2 L^2}{12 R_r}. \tag{B2}$$

The radiation resistance of a short dipole is [20]

$$R_r = \frac{2\pi\eta L^2}{3\lambda^2}. \tag{B3}$$

Substitution of eq (B3) into eq (B2) yields the desired final result:

$$< P_r >= \frac{1}{2}\frac{E_0^2}{\eta}\frac{\lambda^2}{4\pi}, \tag{B4}$$

which is identical to eq (66) for general antennas. The polarization mismatch factor of one half is particularly clear for the electric dipole antenna because $S_{r\beta} = 0$.

The idealized electric-dipole theory in this appendix does not apply directly to electric-field probes because most probes are terminated with a high impedance rather than a matched load. In this case the relevant quantity is the open-circuit voltage V_i as discussed in Section 4.2. Typically only the field magnitude is sensed:

$$|V_i| = L|E_z| \tag{B5}$$

and the effective length is determined by calibration rather than theory. Experimental comparisons [8] of electric-field components with field probes and received power with larger antennas have been consistent with the theory in Section 3.

APPENDIX C. SMALL LOOP ANTENNA

The other electrically small antenna of practical interest is the small loop. For a small loop of area A centered on the z axis in the xy plane as shown in figure 22, the components of the receiving function are

$$S_{r\alpha} = 0 \quad \text{and} \quad S_{r\beta} = \frac{-i\omega\mu A \sin\alpha}{2\eta R_r}. \tag{C1}$$

The results in eq (C1) are obtained by: (1) determining the magnetic flux density penetrating the loop, (2) multiplying by $-i\omega$ to determine the induced voltage, and (3) dividing by $2R_r$ to determine the current induced in a matched load. If eq (C1) is substituted into eq (63), the angular integration can be carried out to obtain

$$< P_r >= \frac{E_0^2\omega^2\mu^2A^2}{12\eta^2R_r}. \tag{C2}$$

The radiation resistance of a small loop is [20]

$$R_r = \frac{2\pi\eta}{3}\left(\frac{kA}{\lambda}\right)^2. \tag{C3}$$

Substitution of eq (C3) into eq (C2) yields the desired final result:

$$< P_r > = \frac{1}{2}\frac{E_0^2}{\eta}\frac{\lambda^2}{4\pi}. \tag{C4}$$

which is identical to eq (66) for general antennas and eq (B4) for a short electric dipole. The polarization mismatch factor of ½ is also clear for a small loop because $S_{r\alpha} = 0$.

APPENDIX D. CHAMBER TIME CONSTANT

The chamber time constant is of interest for transient applications and for measurement of Q [7],[44]. Consider first the case where a cw source is instantaneously turned off. By equating the change in cavity energy U to the negative of the dissipated power times a time increment dt, we obtain the differential equation

$$\mathrm{d}U = -P_d \, \mathrm{d}t. \tag{D1}$$

Equation (91) can be used to replace P_d in eq (D1):

$$\mathrm{d}U = -(\omega U / Q)\,\mathrm{d}t = -\frac{U}{\tau}\mathrm{d}t, \tag{D2}$$

where the time constant $\tau = Q/\omega$. The initial condition is $U = U_0$ at $t = 0$. The solution of eq (D2) with this initial condition is

$$U = U_0 \exp(-t/\tau), \quad t \geq 0. \tag{D3}$$

The closely related case of a turned-on (step modulated) cw source involves the same exponential function and time constant:

$$U = U_0 [1 - \exp(-t/\tau)], \quad t \geq 0. \tag{D4}$$

The average energy density $<W>$ and received power $<P_r>$ follow the same exponential decay or buildup. If the average received power is fit to an exponential curve, the inferred time constant τ can be used to measure the cavity Q [46],[56]:

$$Q = \omega\tau. \tag{D5}$$

This method has the advantages that it does not require a knowledge of the chamber volume and it is less affected by antenna efficiency and mismatch.

Table 1. Mode properties for a rectangular cavity.

Designation	Restrictions	Nonvanishing components	Number of modes
TM_{lmn}	$l\geq 1$, $m\geq 1$, $n\geq 1$	E_x, E_y, E_z, H_x, H_z	$N_1(k)$
TE_{lmn}	$l\geq 1$, $m\geq 1$, $n\geq 1$	E_x, E_y, H_x, H_y, H_z	$N_2(k)$
TM_{lm0}	$l\geq 1$, $m\geq 1$, $n=0$	E_z, H_x, H_y	$N_3(k)$
TE_{0mn}	$l=0$, $m\geq 1$, $n\geq 1$	E_x, H_y, H_z	$N_4(k)$
TE_{l0n}	$l\geq 1$, $m=0$, $n\geq 1$	E_y, H_x, H_z	$N_5(k)$

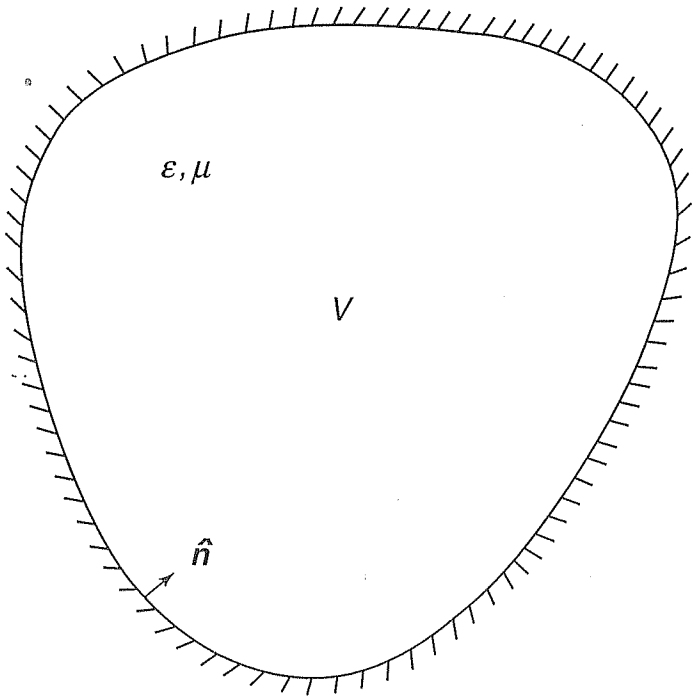

Figure 1. Cavity of volume V with perfectly conducting walls.

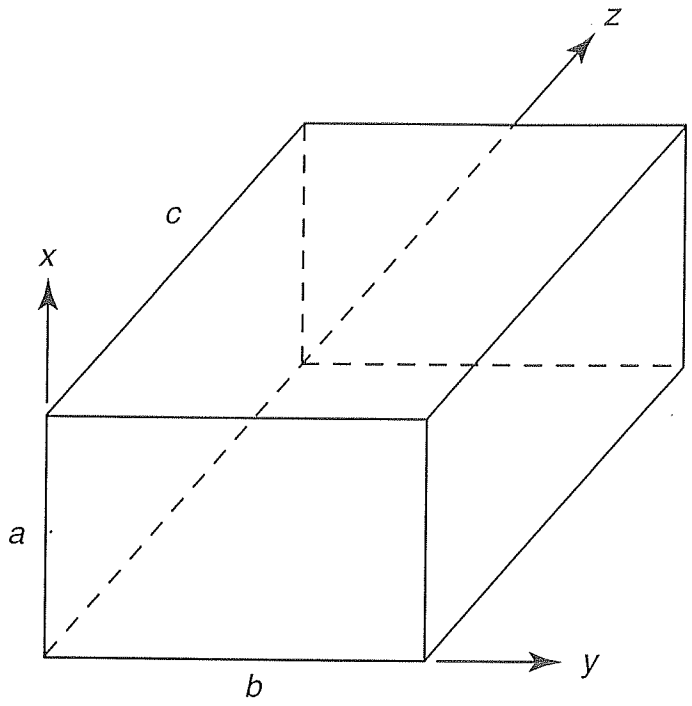

Figure 2. Empty rectangular cavity with dimensions $a \times b \times c$.

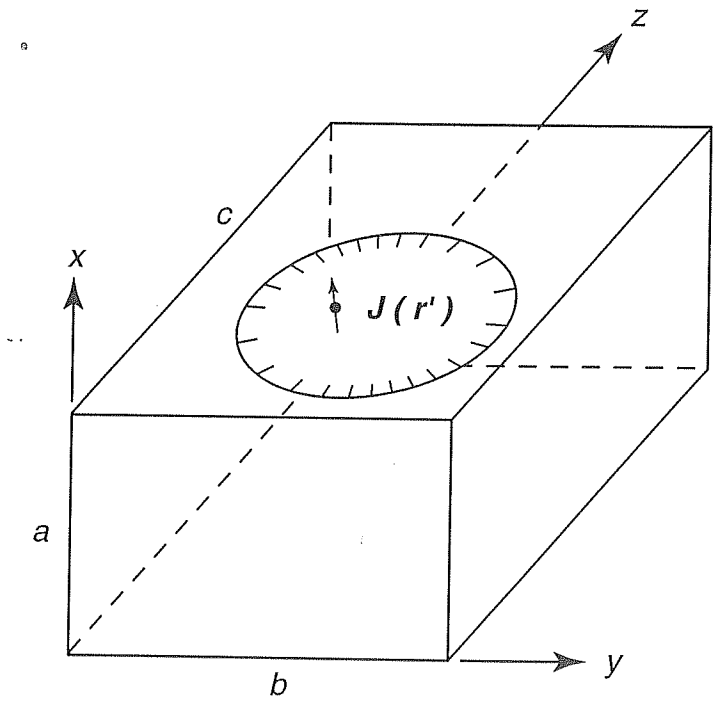

Figure 3. Source current distribution $\boldsymbol{J}(\boldsymbol{r}')$ in a rectangular cavity.

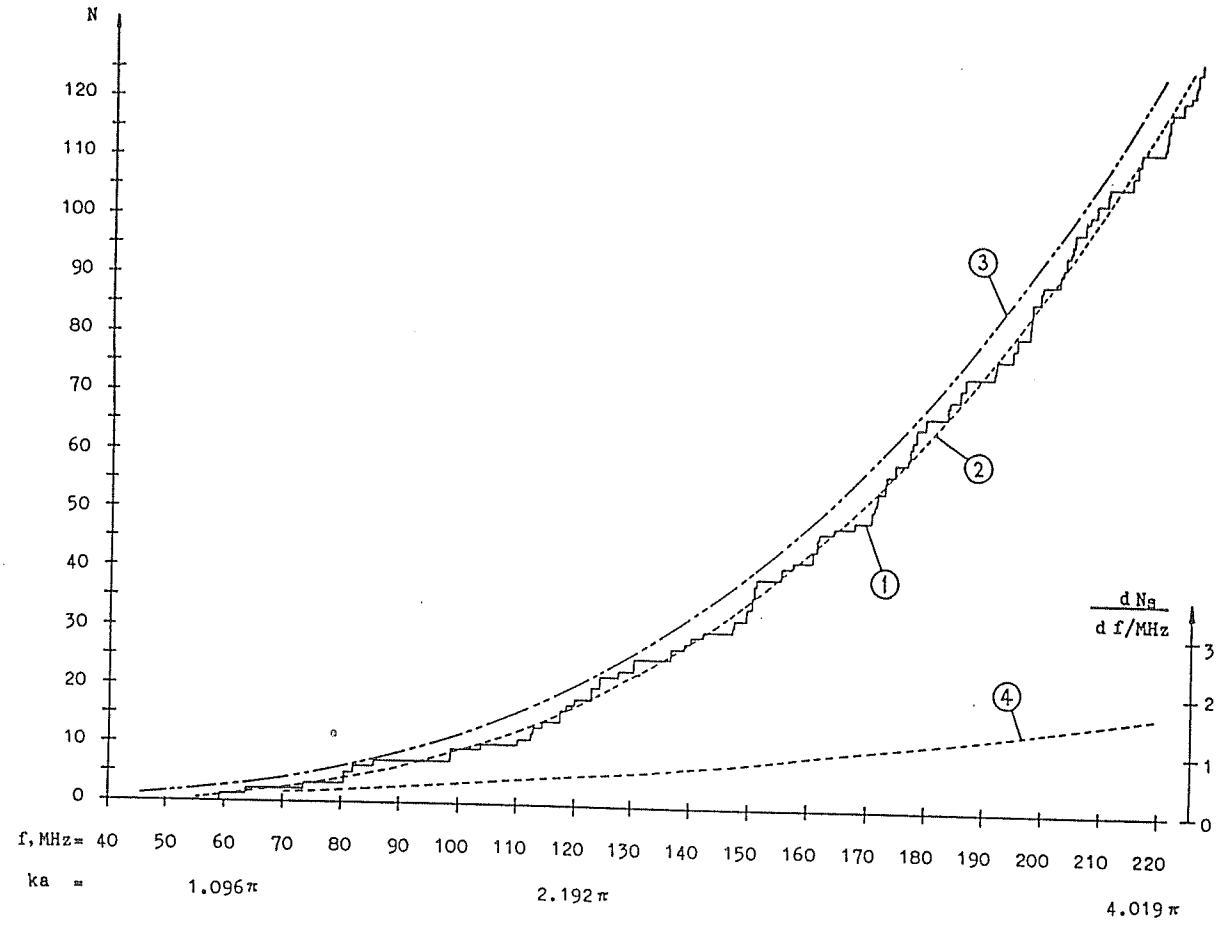

Figure 4. Mode number (curve 1), smooth approximation to the mode number (curve 2), Weyl approximation to the mode number (curve 3), and smooth mode density (curve 4) for the NIST reverberation (2.74 m × 3.05 m × 4.57 m).

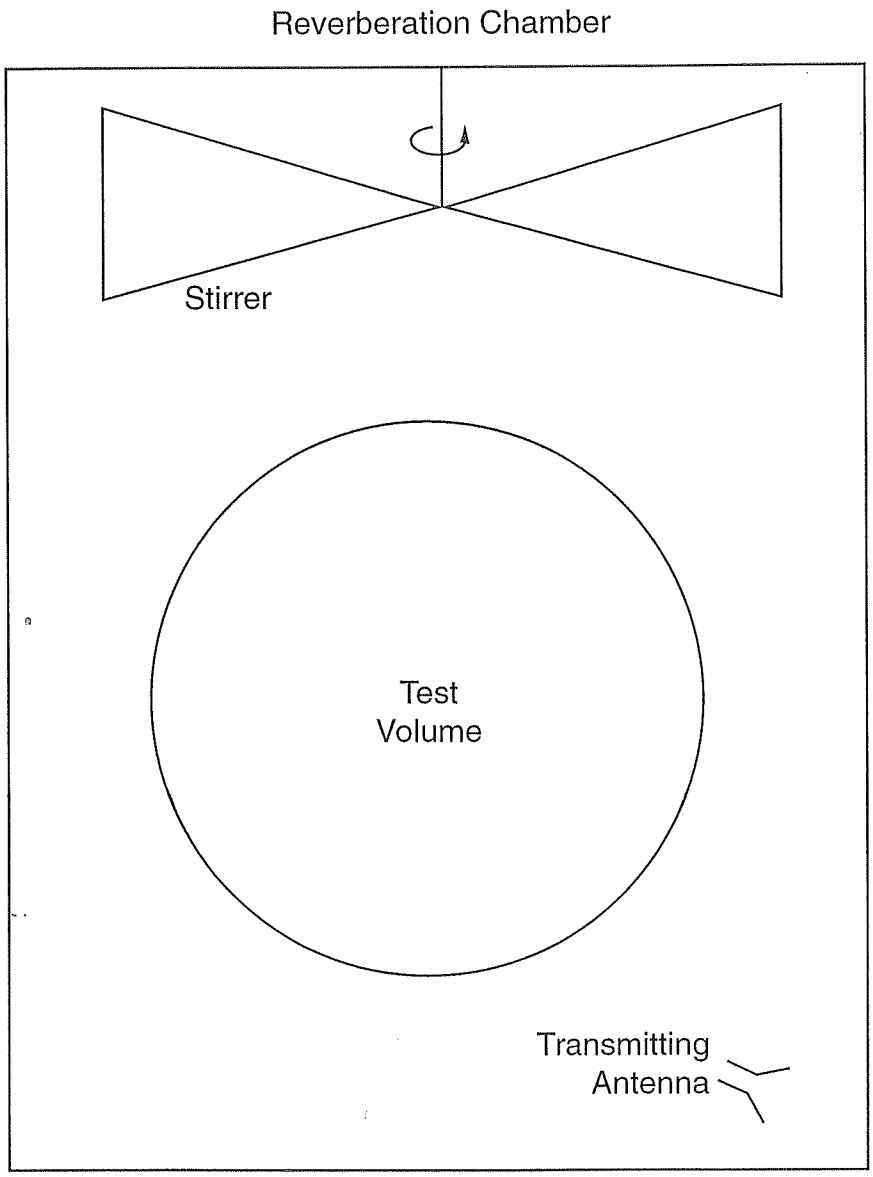

Figure 5. Transmitting antenna in a reverberation chamber with a mechanical stirrer.

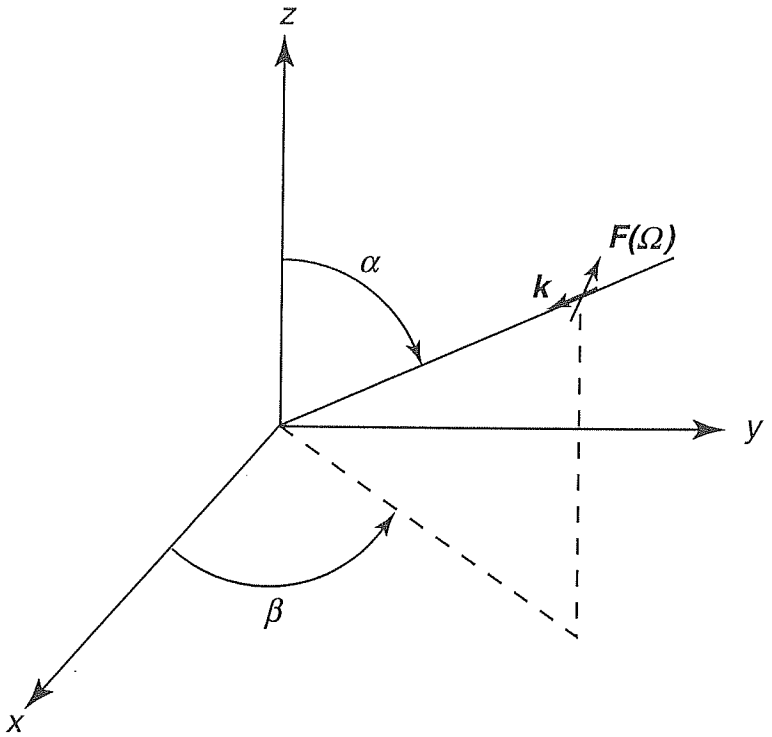

Figure 6. Plane-wave component $F(\Omega)$ of the electric field with wavenumber $\boldsymbol{k}$.

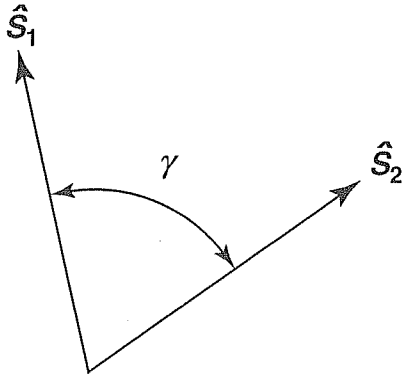

Figure 7. Unit vectors, $\hat{s}_1$ and $\hat{s}_2$, with an angular separation γ.

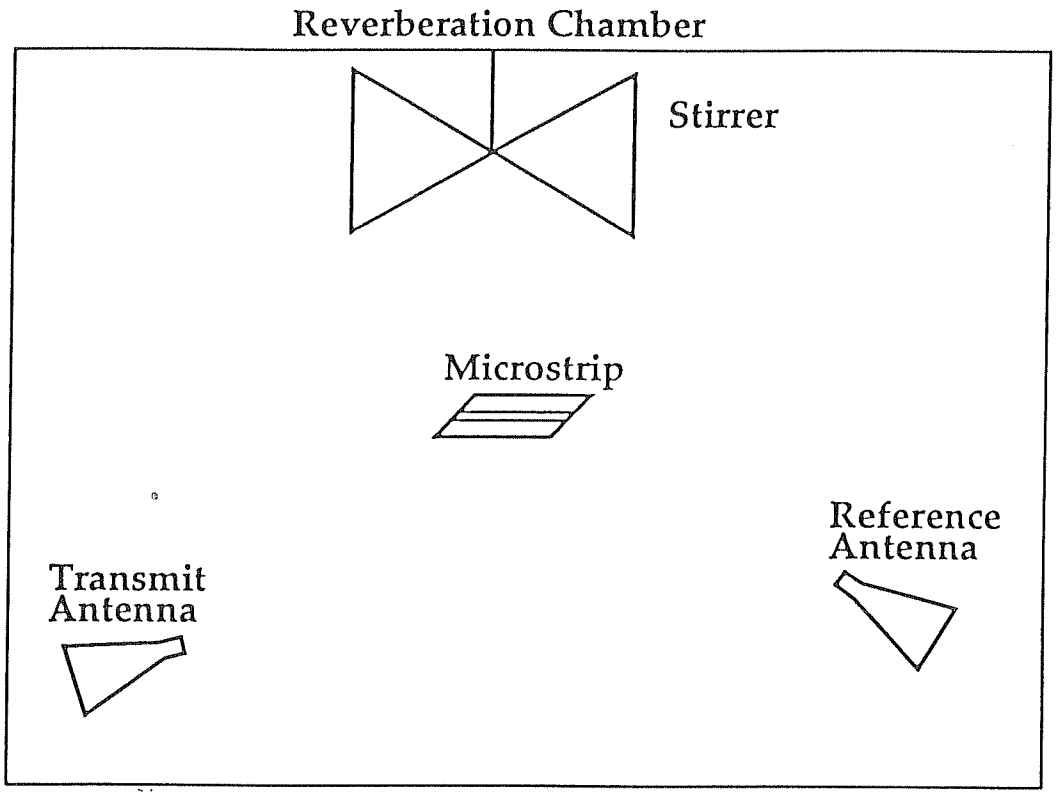

Figure 8. Test setup for immunity measurement of a microstrip transmission line in a reverberation chamber.

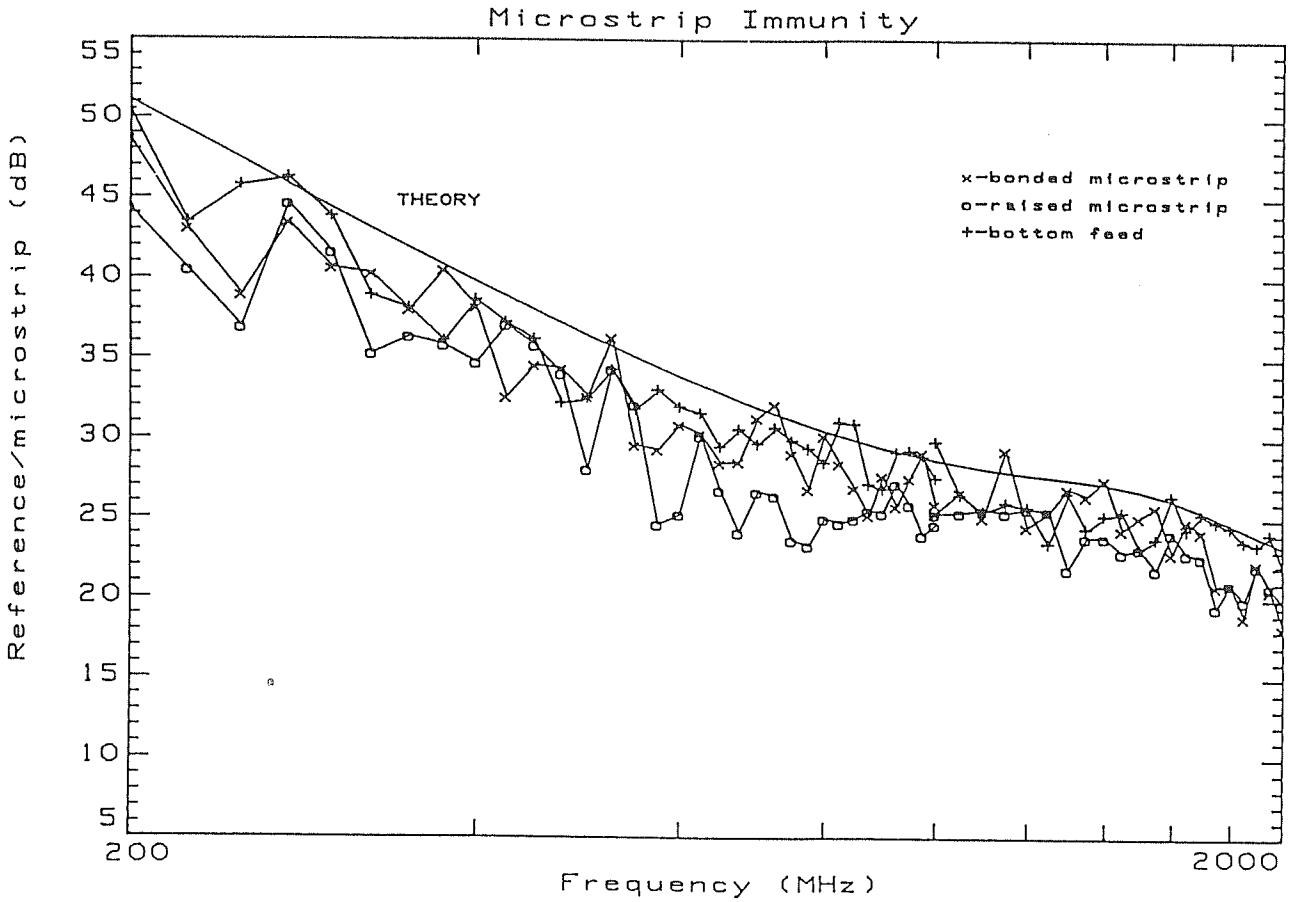

Figure 9. Comparison of theory with three measurements of the radiated immunity of a microstrip transmission line [40] in the NIST reverberation chamber.

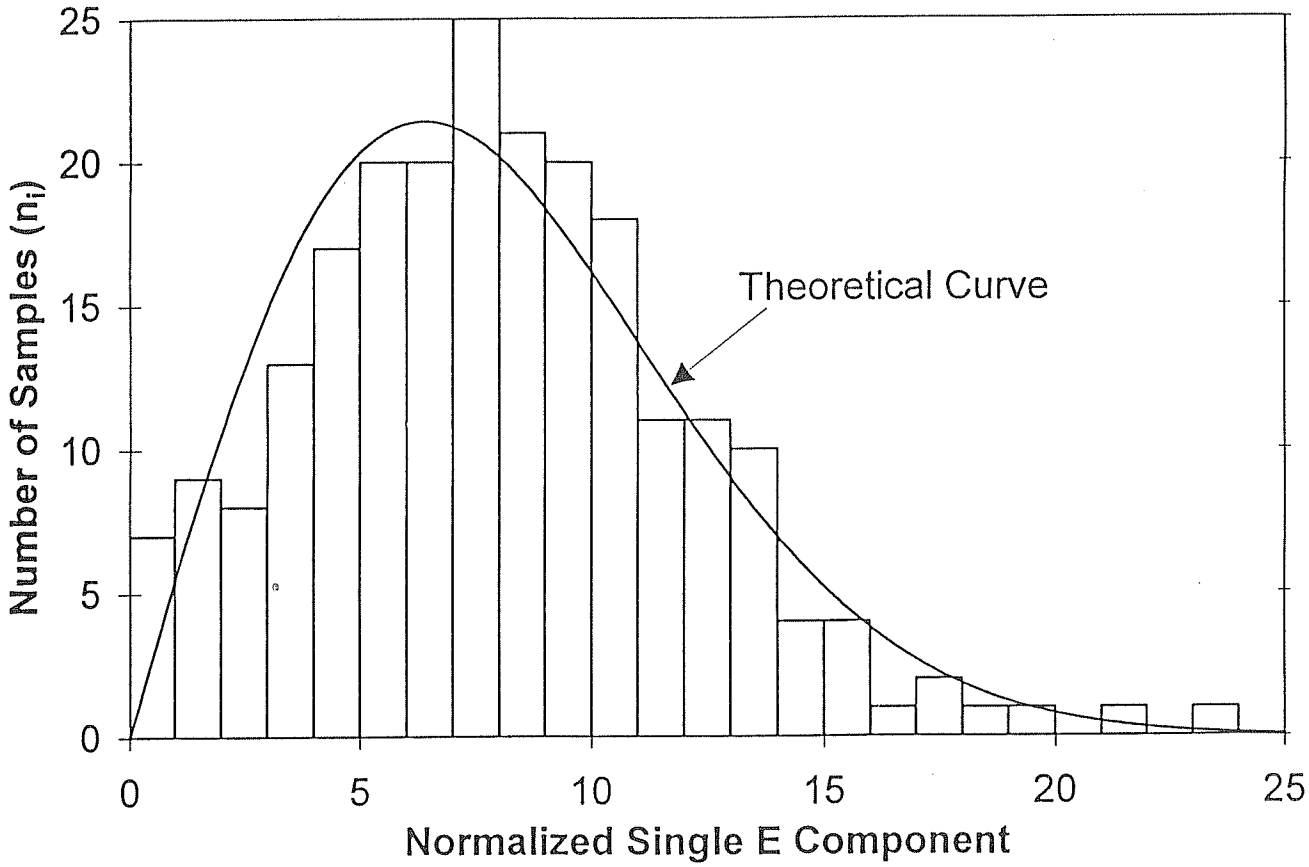

Figure 10. Comparison of the measured probability density function of a single rectangular component of the electric field [8] with theory (Rayleigh distribution).

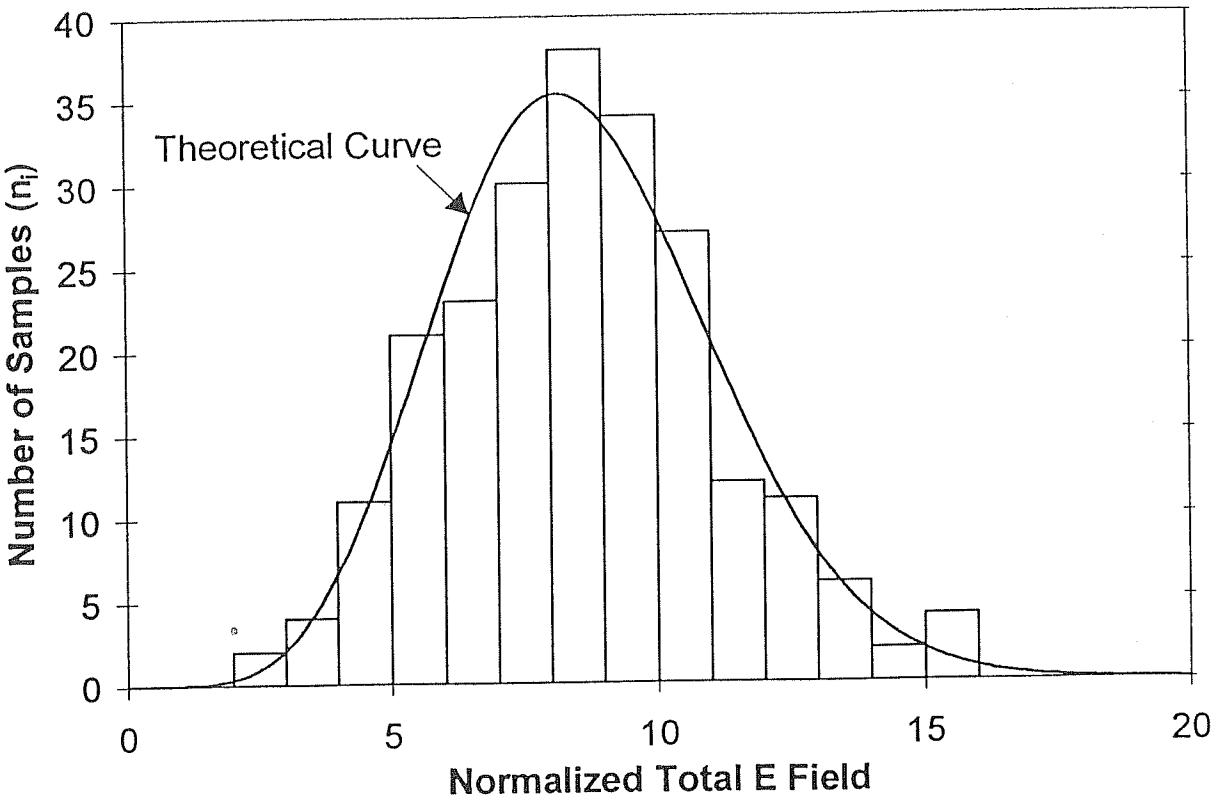

Figure 11. Comparison of the measured probability density function of the total electric field [8] with theory (chi distribution with 6 degrees of freedom).

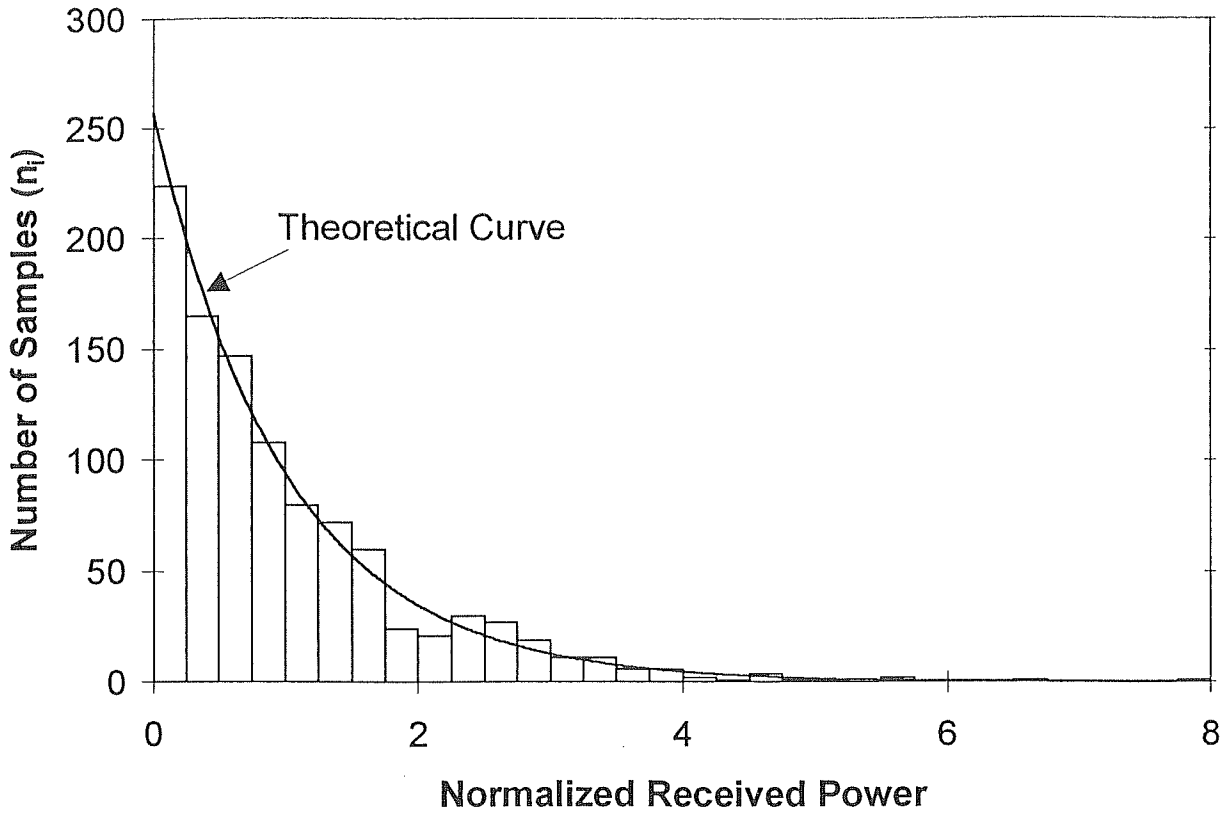

Figure 12. Comparison of the measured probability density function of received power [8] with theory (exponential distribution).

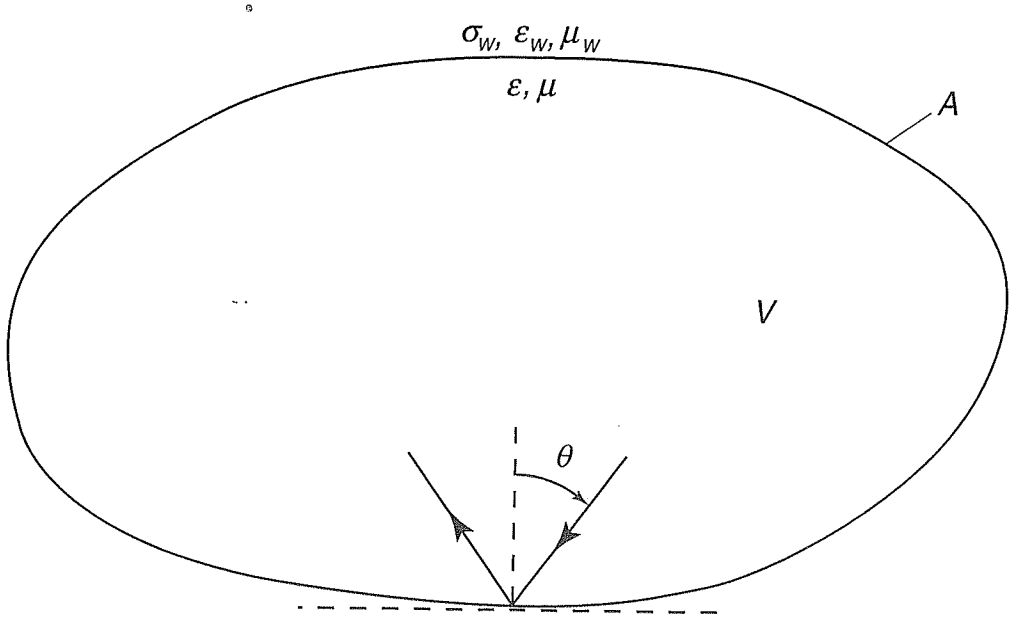

Figure 13. Plane-wave reflection from an imperfectly conducting wall of a reverberation chamber.

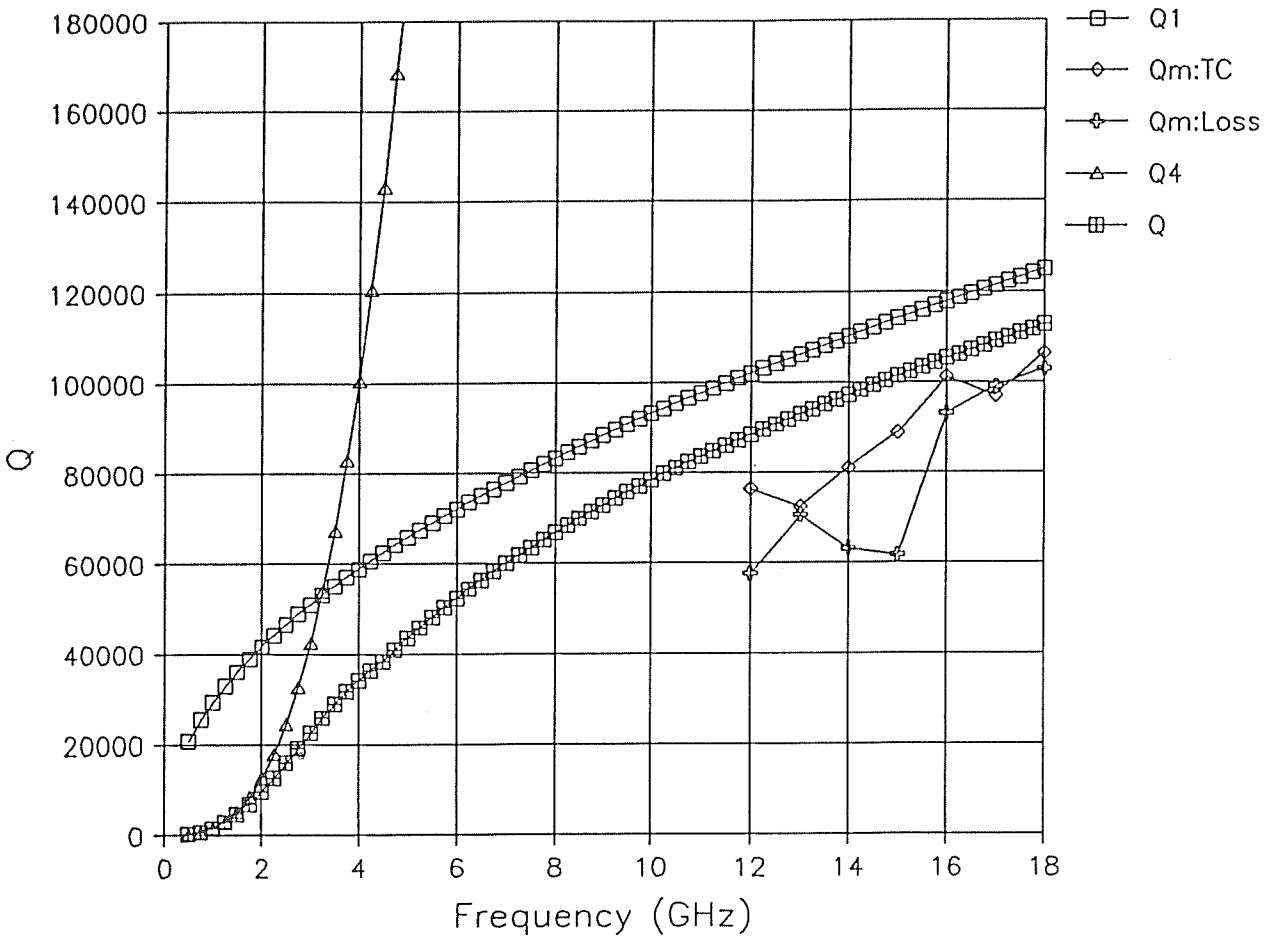

Figure 14. Comparison of Q measured by power ratio (Qm:Loss) and decay time (Qm:TC) with Q calculated from eq (97) for an aluminum cavity [44]. The theoretical values for wall loss (Q1) and receiving antennas (Q4) are also shown.

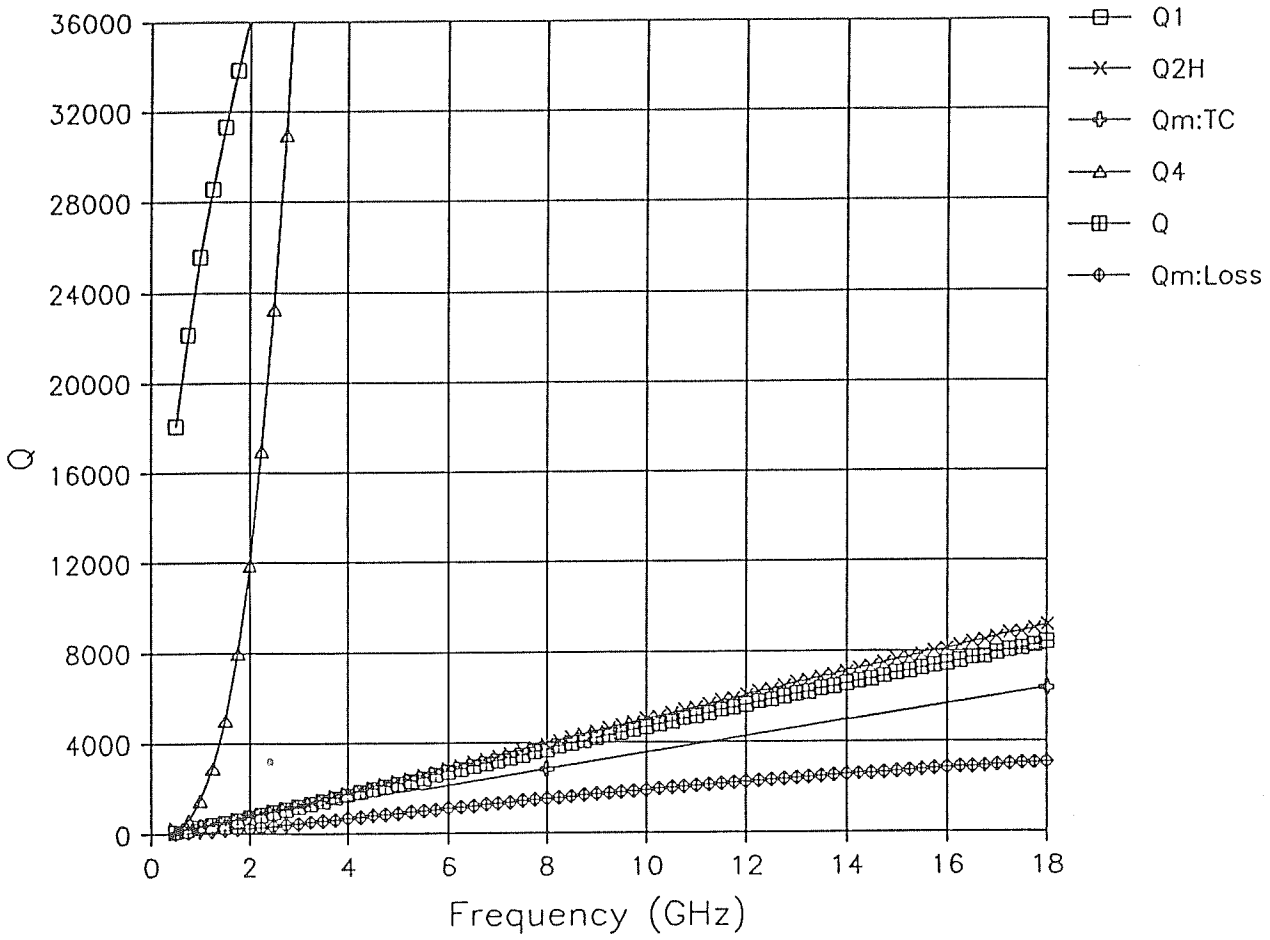

Figure 15. Comparison of Q measured by power ratio (Qm:Loss) and decay time (Qm:TC) with Q calculated from eq (97) for an absorber-loaded aluminum cavity [44]. The theoretical values for wall loss (Q1), absorption by salt-water spheres (Q2H), and receiving antennas (Q4) are also shown.

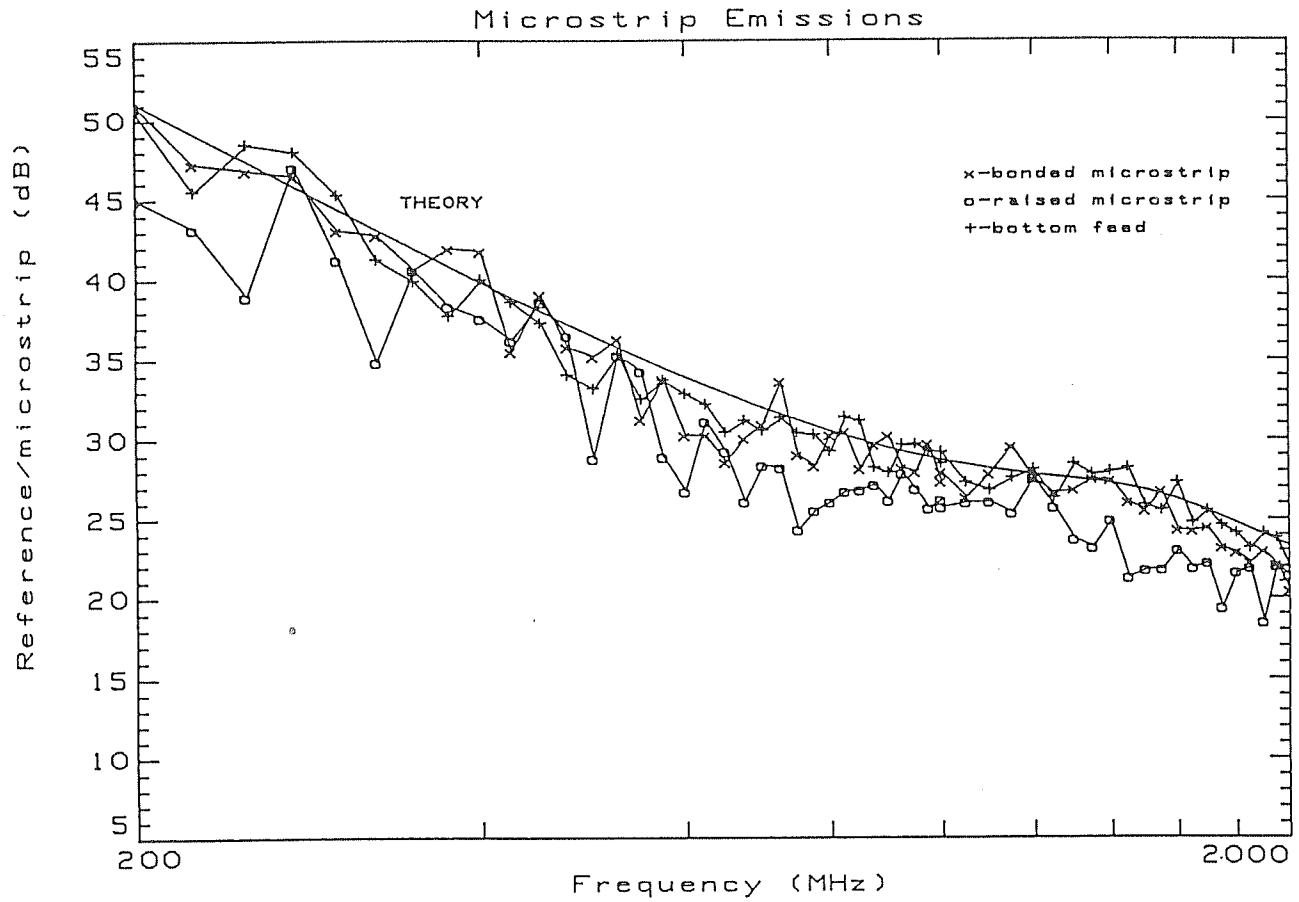

Figure 16. Comparison of theory with three measurements of the radiated emissions of a microstrip transmission line [40] in the NIST reverberation chamber.

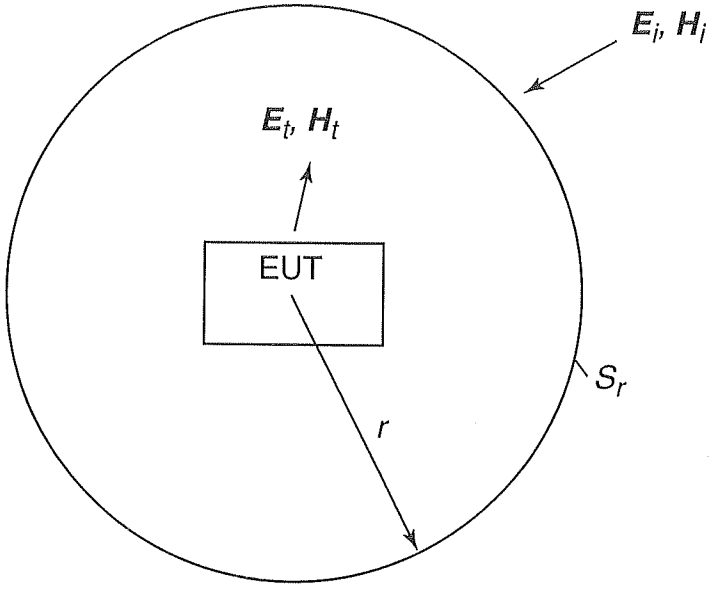

Figure 17. Equipment under test (EUT) radiating fields E_t, H_t (emissions measurement) or illuminated by by fields E_i, H_I (immunity measurement).

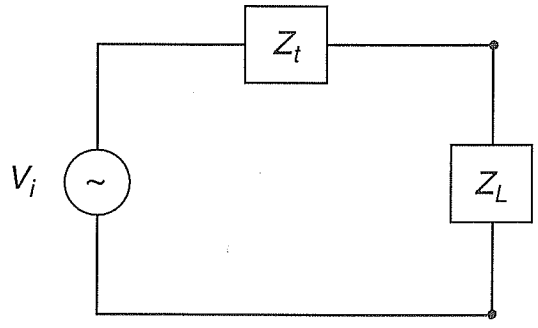

Figure 18. Thevenin equivalent circuit for a single port in equipment under test.

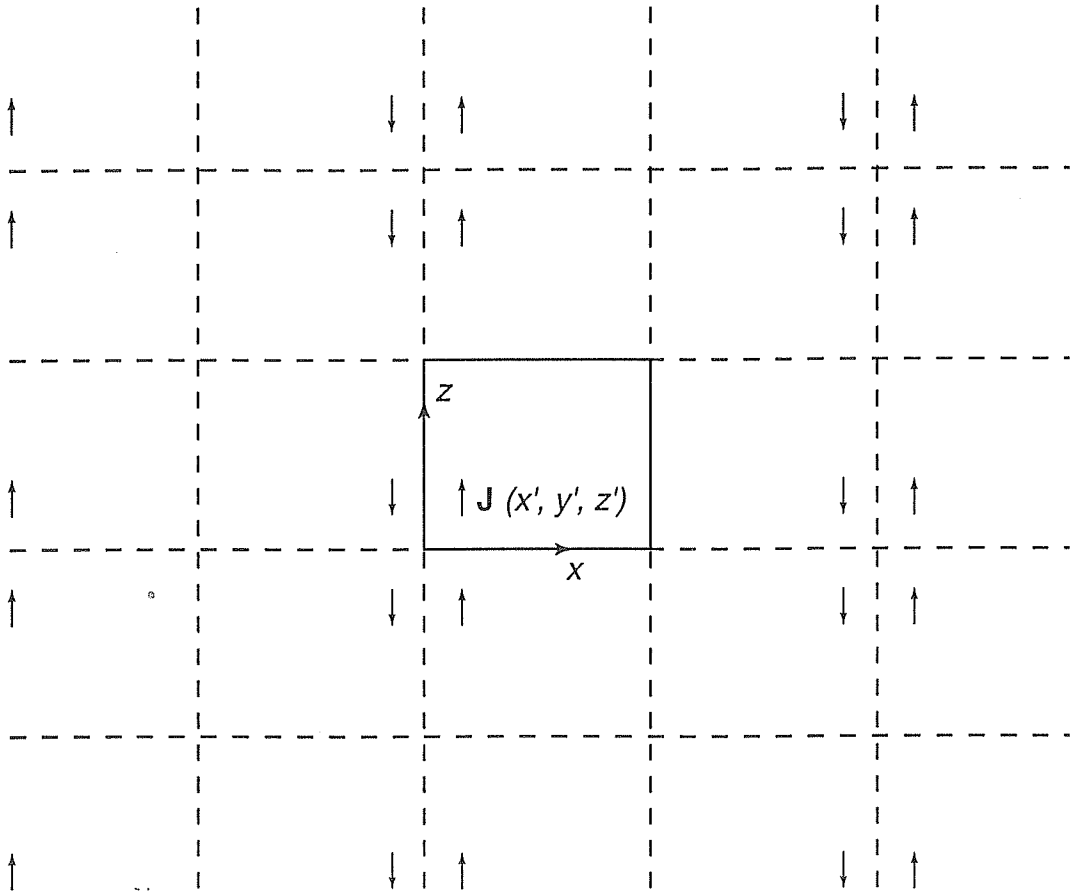

Figure 19. Multiple images for a z-directed dipole source in a rectangular cavity.

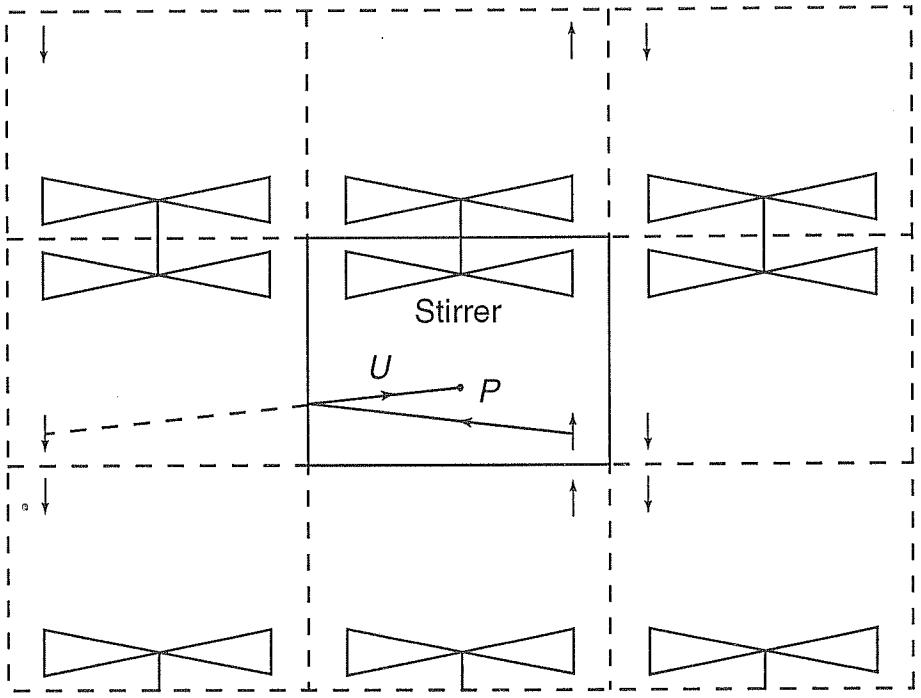

Figure 20. Images of source and stirrer in a rectangular cavity. The (single-bounce) ray U is not affected by the stirrer (hence contributes to unstirred energy).

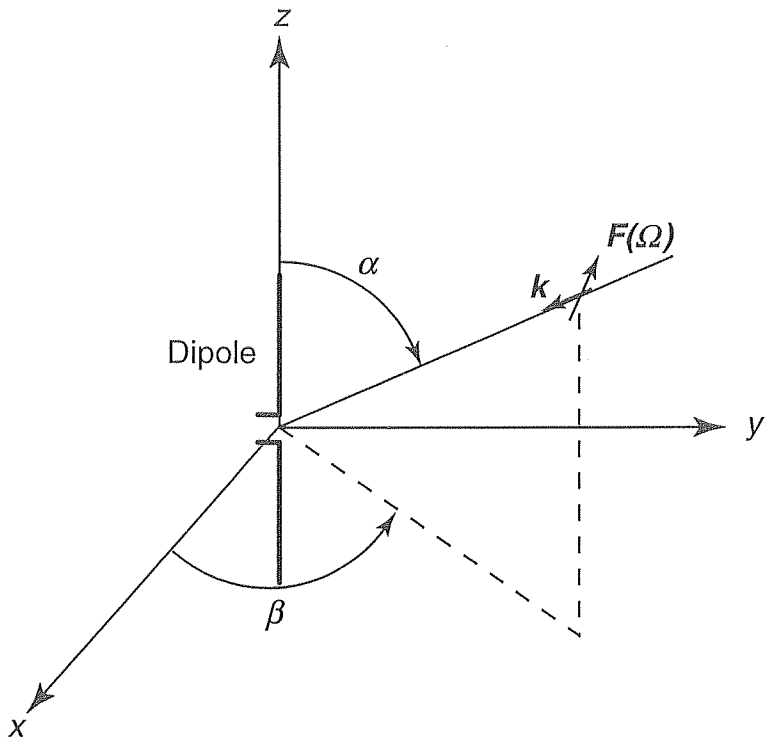

Figure 21. Dipole antenna illuminated by a plane-wave component of the electric field.

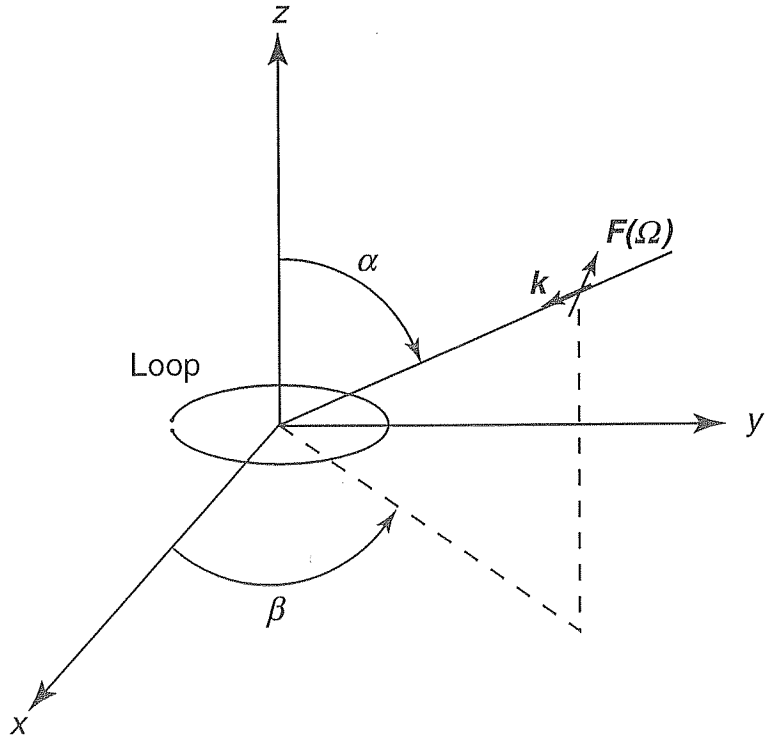

Figure 22. Loop antenna illuminated by a plane-wave component of the electric field.

*U.S. GOVERNMENT PRINTING OFFICE 1998-0-773-022/40123